学位論文

Single-Electron Effects in Small Tunnel-Junction Arrays

（微小トンネル接合のアレイにおける単一電子効果）

平成５年１２月博士（理学）申請

東京大学大学院理学系研究科
物理学専攻

神田　晶申

Thesis

Single-Electron Effects in Small Tunnel-Junction Arrays

Akinobu Kanda

Department of Physics
Graduate School of Science
University of Tokyo

December 1993

Contents

Chapter 1

Introduction

1.1 What is Single-Electron Effect?

Tunneling is quantum-mechanical transmission of an electron across a potential barrier.

In tunnel junctions, tunneling becomes more frequent as an overlap of the electron wavefunctions in both electrodes gets larger. This shows that the wave properties of electrons cause the tunneling. On the other hand, because of the particle properties of electrons, i.e. because electrons tunnel one by one, single-electron tunneling changes the electrostatic energy of the system by the amount of

$$\Delta E_C = \frac{(Q \pm e)^2}{2C} - \frac{Q^2}{2C}, \tag{1.1}$$

where Q is the charge of the junction before the tunneling and C is the capacitance of the junction. In ordinary macroscopic tunnel junctions, this quantity is much smaller than the thermal energy $k_B T$, and hence the influence of the change of the charging energy can be ignored. On the other hand, in small tunnel junctions with capacitance below 10^{-15}F, ΔE_C becomes larger than 1K and the charging energy affects the transport properties of the junction at low temperatures. The effects of charging energy on the transport properties of tunnel junctions are called the "charging effects"or the "single-electron effects".

There are three elementary phenomena in the single-electron effects:

- Tunneling which increases the electrostatic energy of the system is suppressed (the Coulomb blockade).
- When the junction is current (I) biased, the voltage oscillates at the frequency $f_{\rm SET} = I/e$ (Single-Electron Tunneling oscillation (SETO)).
- In current-biased Josephson junctions, the voltage oscillates at the frequency $f_{\rm B} = I/2e$ due to the Cooper-pair tunneling (Bloch oscillation).

In this thesis, we are devoted to the single-electron effects in artificial small tunnel-junction arrays. The following three subjects are studied:

1. Single-electron tunneling in one-dimensional arrays of small tunnel junctions,
2. Influence of dissipation in one-dimensional arrays of small Josephson junctions,
3. Electrical transport in two-dimensional arrays of small Josephson junctions.

1.2 Organization

This thesis is organized as follows: In chapter 2, we describe the sample fabrication technique and the measurement methods. Chapters 3, 4 and 5 correspond to the subjects 1,2 and 3, respectively. In chapter 6, we give conclusion.

Chapter 2

Experiments

2.1 Sample Fabrication

For the fabrication of the tunnel junctions, we employed the shadow deposition technique proposed by Dolan *et al.*[1] combined with the electron beam lithography. Since all of the depositions are achieved in one single vacuum cycle, we can expect that the tunnel barrier contains relatively little contamination and we can control its thickness easily. Moreover, in principle, we can make junctions with very small area by adjusting the angle of evaporation.

Small tunnel junctions used in this experiment consist of aluminum and its oxide. Aluminum is suitable material for tunnel junctions partly because it forms not grains but continuous film after several 10nm vacuum deposition at room temperature and partly because its oxide film has no pinhole.

Below we describe the fabrication process of small tunnel junctions in detail.

Preparation of Substrates We used 10mm × 5mm silicon wafers with Au contact pads as the substrates. They were spin-coated with two-layer electron-beam resist.(Fig.2.1.1(a)) The first resist (the bottom layer) was PMMA/PMAA (90:10) copolymer dissolved in 1-acetoxy-2-ethoxyethane(ECA). This was spun on the substrates at 3000r.p.m. for 60sec.

and then baked at 190°C for 20min. The second resist (the top layer) was OEBR1000 (Tokyo Ouka) dissolved in ECA, which was spun at 3000r.p.m. for 60sec. Then the substrates were baked at 170°C for 20min. The resulted thickness of the resists was about 450nm.

Electron-Beam Lithography The electron-beam lithography system was ELIONIX ELS3300LB(I). For the exposure of small areas, bias voltage was 20kV, beam current 14-20pA and a dose 110-150$\mu C/cm^2$.

After the exposure, the substrates were developed in two developers. Firstly it was developed in OEBR1000 developer at 23°C for 5-20 sec. and then rinsed in 2-propanol for 60sec. Secondly it was developed in etylalchole dissolved by 2-propanol at 23°C for 20-90sec. and then rinsed for 60sec. Finally the chip was washed in water. The first developer develops both resists, whereas the second only the bottom resist.

By the use of these selective developers, the "suspended bridge"structures shown in Fig.2.1.1(b) were fabricated between the patterns with short distances.

Vacuum Deposition Aluminum was thermally evaporated in a diffusion-pumped vacuum chamber at a pressure of $2-4\times10^{-7}$ torr. After the first evaporation, oxygen at the pressure of $10^{-2}-10^{-1}$torr was introduced into the vacuum chamber for 5-60 sec. to form the tunnel barrier. Then we evaporated Aluminum from different direction by tilting the substrates. After these procedures, tunnel junctions were made below the suspended bridges. The thickness of the electrodes was 300 nm. The redundant metal was lifted off in acetone. (Fig.2.1.1(c)(d))

2.2 Measurement

2.2.1 Cryostats

The samples were cooled down to 30mK in dilution refrigerators. The substrates were fixed in the mixing chamber made from Stycast 1266 epoxy. We attached the four current- and voltage-leads to the contact pads on the substrates by the silver paste or by the solder made from InSn, which has low melting temperature. Temperature was measured by a carbon resistor placed near the substrates in the mixing chamber. The microwave was fed via a coaxial cable to a rod antenna placed close to the samples. In the experiments described in chapters 3 and 5, the magnetic field up to 4T was applied parallel to the junctions by a superconducting solenoid. In experiments described in chapter 4, magnetic field up to 1T was applied by an electromagnet placed outside the dewar.

2.2.2 Measuring Circuits

One-Dimensional Arrays The measuring circuit used for the experiments described in chapters 3 and 4 is shown in Fig.2.2.1. To minimize the pick-up of external noise, the biasing circuit and the preamplifiers were battery-powered and set in a shielded box. When measuring the current-voltage characteristics, we swept the current by charging the capacitor b. The sweep rate was controlled by the resistance a. When measuring the differential resistance, we superimposed a modulation signal from a lock-in amplifier via a transformer c. The modulation frequency was 5Hz in the experiments described in chapter 3 and 34Hz in chapter 4. The current was determined by the voltage of the resistor d. Each of the preamplifiers used for the current and voltage measurements was composed of three low noise operational amplifiers. The outputs of the preamplifiers were recorded by a X-Y chart recorder and they were digitized after the experiments. In the experiments described in chapter 3, the *RC* low-pass filters with the cutoff frequency of 16kHz were inserted into

the measuring wires. They were attached to a cold plate of 100mK. Metal-film resistors and film capacitors were used as the components of these filters to prevent the change of the properties at low temperatures. In the experiments described in chapter 4, we inserted the metal-film chip resistors of 22kΩ into the leads in the mixing chamber, which formed low-pass filters with the stray capacitance of the leads.

Two-Dimensional Arrays In the experiments of two-dimensional arrays described in chapter 5, we collected data by a personal computer optically connected to the instruments. The measuring circuit is shown in Fig.2.2.2. The preamplifier used for the voltage measurement was composed of three low noise operational amplifiers. In order to measure the current of the order of 1pA flowing through the samples with very high resistance correctly, we minimize the leak current by the following treatments: 1) we inserted an operational amplifier in the current leads between the sample and the ammeter to make the potential of this lead zero. 2)Each of the operational amplifiers connected to the sample had a high input impedance and a very low input bias current. Between the samples and the instruments such as the current source, the ammeter and the digital voltmeter, we inserted low-pass filters and electromagnetic interference (EMI) filters. Moreover, we inserted metal-film chip resistors of 22kΩ into the leads in the mixing chamber.

Chapter 3

Single-Electron Tunneling in One-Dimensional Arrays of Small Tunnel Junctions

3.1 Introduction

3.1.1 Single-Electron Tunneling in Normal Single Junctions

We consider an electrically-isolated tunnel junction with the tunnel resistance R and the capacitance C. We assume that following conditions are satisfied:

$$T \ll \frac{e^2}{2k_B C}, \tag{3.1}$$

$$R \gg R_Q, R_Q = \frac{h}{4e^2}. \tag{3.2}$$

The condition (3.1) holds if the elementary charging energy for a single electron tunneling $E_C = e^2/2C$ is larger than the thermal energy $k_B T$ so as to suppress tunneling due to thermal excitation. The condition (3.2) holds if the characteristic energy for quantum

fluctuation of the charge is much smaller than E_C. Here the characteristic energy for quantum fluctuation of the charge is related to the decay time of virtual state $\Delta t \sim CR$ by the Heisenberg uncertainty relationship.

Under these conditions, tunneling can be treated as classical stochastic process. From the Fermi's golden rule, the tunneling rate at T=0 is given as follows:[1]

$$\Gamma_{SET} = -\frac{\Delta E_C}{e^2 R}. \tag{3.3}$$

Here ΔE_C is the change of the electrostatic energy by a tunneling event:

$$\Delta E_C = \frac{(Q \pm e)^2}{2C} - \frac{Q^2}{2C}. \tag{3.4}$$

If ΔE_C is positive, i.e.,

$$-\frac{e}{2} < Q < \frac{e}{2}, \tag{3.5}$$

any tunneling is suppressed. This suppression is called the "Coulomb blockade "of tunneling.[2]

Next, let us consider the junction biased by a constant external current I at $T = 0$. Because Q is the electrode's surface charge resulting from deviation of the electron distribution from the ion (crystal lattice) distribution, it does not takes discrete values ne (n:integer) but continuous value. When the external charge is inserted into the junction at a small rate I, the tunneling of electron is prohibited due to the Coulomb blockade until Q reaches $e/2$. As soon as Q exceeds $e/2$, the tunneling probability increases and an electron tunnels. After the tunneling, Q becomes less than $e/2$ and the junction is recharged as shown in Fig.3.1.1. This charging-tunneling process repeats with the average frequency

$$f_{SET} = I/e. \tag{3.6}$$

[1]The relation between the tunnel resistance R, the density of states of the left (right) electrode D_L (D_R) and the tunneling matrix of the electron transfer $|\,T\,|$ is given by

$$R^{-1} = \frac{4\pi e^2}{\hbar} D_L D_R \,|\,T\,|^2 .$$

Here we assume that D_R, D_L and $|\,T\,|$ are indepedent of the energy near the Fermi surface.

Here, although the tunneling at $V > e/2$ is fully stochastic, the tunneling becomes "pseudoperiodic"due to the Coulomb blockade. Consequently, the voltage of the junction oscillates at a considerably large amplitude in the same frequency. This is called "Single-Electron Tunneling Oscillations (SETO)".

The SETO affects the dc current-voltage (I-V) characteristic considerably. At a low bias current where tunneling is influenced by the Coulomb blockade, it is shown that $V \propto \sqrt{I}$. When the time-average of the voltage exceeds e/C, the Coulomb blockade does not occur and the I-V characteristic approaches the linear asymptotes, $V = RI + e/2C$ as shown in Fig 3.1.2.

When we impose dc current plus ac current of frequency f_{ext}, the SETO is phase-locked. Because of a frequency pulling effect between the SETO and the ac current, there appear voltage spikes at current

$$I = \frac{n}{m} e f_{ext}, \tag{3.7}$$

where n and m are integer.[2]

It is difficult to observe the SETO in single junctions. The reason is that both the large capacitance of the measurement leads and the high resistance of the junction make the junction voltage-biased. In a voltage-biased junction, the Coulomb blockade and the SETO should not occur and hence the I-V characteristic should become ohmic, because tunneling does not changes the electrostatic energy of the junction. In order to prevent the junction being voltage-biased, resistors with very high resistance must be inserted in the measurement leads very close to the junction. One way is to deposit resistive alloy such as NiCr or AuCu.[3] But it seems difficult to obtain sufficiently large resistance because the resistivity of such alloy is much smaller than R_Q. An easier way is to connect multiple junctions one-dimensionally. In one-dimensional arrays, every junction can be effectively

[2]This is similar to the Shapiro steps in Josephson junctions.[4] For a review on the frequency pulling effects in Josephson junctions, see for instance ref.[5].

current-biased by the high resistance of the other junctions.

3.1.2 Single-Electron Tunneling in One-Dimensional Arrays of Small Tunnel Junctions (Soliton Model)

Let us consider $N(\gg 1)$ junctions connected in series.[6][7] We take into account not only the capacitance C but also the self capacitance C_0 of an electrode between junctions (island-electrode) as shown in Fig.3.1.3. When conditions (3.1) and (3.2) are satisfied, we can interpret the properties of electron transport as the dynamics of single-electron solitons and antisolitons.

The single-electron soliton whose center is on k -th island electrode is expressed as follows:

$$\phi_i = -\frac{e}{C_{\rm eff}} \exp\left(-\frac{|\, i-k\,|}{\lambda}\right). \tag{3.8}$$

Here ϕ_i is the potential of i-th island-electrode and

$$C_{\rm eff} = (C_0^2 + 4CC_0)^{1/2}, \tag{3.9}$$

$$\lambda^{-1} = \operatorname{arccosh}\left(1 + \frac{C_0}{2C}\right). \tag{3.10}$$

These equations express polarization of neighboring island-electrodes by an excess charge on k-th island-electrode. The range of polarization is characterized by λ. Because the functional dependence of equation (3.8) is unchanged by the tunneling and by the presence of other electrons, the name "single-electron soliton "is used.

Next, we connect the each end of the array to a constant voltage source. When the potentials of the end-electrodes are equally increased, solitons are injected from both ends of the array. Because solitons are mutually repulsive, they tend to distribute at nearly equal distance and form one-dimensional Wigner lattice, whose periodicity is distorted by the discreteness of the junctions. The current induced by the difference of the potentials

is interpreted as the parallel movement of this Wigner lattice. Therefore, the soliton motion exhibits considerable degree of space and time correlation, resulting in the voltage oscillation at low current and at low temperatures with the average frequency,

$$f_{\rm SET} = I/e. \tag{3.11}$$

According to the numerical simulation by Likharev *et al.*[6][7], when dc voltage plus ac voltage with frequency $f_{\rm ext}$ is imposed, there appear voltage plateaus in I-V characteristic at current

$$I = nef_{\rm ext}, \quad n{:}\text{integer}. \tag{3.12}$$

This is attributed to the frequency pulling effect.

The shape of the dc I-V characteristic at $T = 0$ is different from that of single junctions. Because solitons have the positive energy

$$E = \frac{e^2}{2C_{\rm eff}}, \tag{3.13}$$

non-zero voltage is needed for injection of a soliton into the array. The threshold voltage $V_{\rm t}^{\rm 1D}$ depends on the average potential of the left and the right ends of the array and its maximum value, $V_{\rm t0}^{\rm 1D}$, is given as

$$V_{\rm t0}^{\rm 1D} = \frac{e}{C(\exp\lambda^{-1} - 1)}. \tag{3.14}$$

Below $V_{\rm t}^{\rm 1D}$ current does not flow.

At high voltages, the I-V curve approaches linear asymptotes.

$$V = NRI + V_{\rm off}^{\rm 1D}, \tag{3.15}$$

$$V_{\rm off}^{\rm 1D} = \frac{e}{C} N(\exp\lambda^{-1} + 1)^{-1}. \tag{3.16}$$

3.2 Results and Discussion

One-dimensional arrays of small tunnel junctions with junction area $0.1 \times 0.08(\mu\text{m})^2$ were fabricated. The tunneling resistance of each junction was of the order of $10^5 - 10^6\Omega$, which is so large that the effect of dissipation can be ignored.[3] The island-electrodes were 0.2μm long, 0.1μm wide and 30nm thick. Because of the RC cut-off frequencies determined by the capacitance of the measuring leads and the resistance of the arrays, the biasing modes of constant-current and constant-voltage selected at the external circuit can be meaningful only below $\approx$100Hz. The current which corresponds to the SETO of 100Hz is much smaller than the noise level of current. Thus the measurement have been always done in the voltage-biased mode irrespective of the external biasing modes.

3.2.1 Effects of Array Length on the Coulomb Blockade and the SETO

The broken curve in Fig.3.2.1 is the dc I-V characteristic of the array of 31 junctions (sample A) in zero magnetic field. The temperature was 0.04K. Here the Al electrodes were superconducting. The absence of zero-voltage Josephson supercurrent is due to the small capacitance and the large tunnel resistance of the junctions; in these conditions the fluctuation of the charge is decreased and then the fluctuation of the phase difference increases because of the Heisenberg uncertainty relationship between the phase difference and the charge.[8]

In order to break the superconductivity, we applied the magnetic field of 3T parallel to the junctions. This value is sufficiently larger than the expected highest critical field due to the paramagnetic depairing ($\approx$ 2T). [9] In Fig.3.2.1, the I-V characteristic is shown with the solid curve in which a Coulomb blockade structure appeared. Two characteristic

[3] In other words, the quantum fluctuation of the charge is much smaller than e.

voltages, V_{off} and V_{t} were observed in this curve where V_{off} is an offset voltage defined in the large voltages as $V = V_{\text{off}} + RI$ and V_{t} is a threshold voltage for the current flow. The current is zero below V_{t} within the noise level of our measurement. V_{off} and V_{t} correspond to $V_{\text{off}}^{\text{1D}}$ and V_{t}^{1D} in the soliton picture respectively. In the experiment, $V_{\text{off}} = 5.7$mV. The value of V_{t} varied between 0.5mV and 1.5mV as shown in Fig.3.2.2. According to the soliton picture, this threshold voltage depends on the average potential of the left and right ends of the array. In the experiment, switching in the external circuit may vary the distribution of offset charges in the circuit,[4] which change the average potential of the array. Substituting $V_{\text{off}}^{\text{1D}} = 5.7$ mV and $V_{\text{t0}}^{\text{1D}} = 1.5$ mV into (3.14) and (3.16), we obtain $C = 3.8 \times 10^{-16}$ F and $C_0 = 2.4 \times 10^{-17}$ F. [5] From these parameters, λ is estimated to be 4 junctions, which is well below the array length.

The I-V characteristic of the array of 5 junctions (sample B) in the magnetic field of 3T is shown in Fig.3.2.3. Here the threshold voltage V_{t} is absent, while the offset voltage V_{off} is seen. Using C_0 of sample A, we obtain $\lambda = 3$ junctions, which is of the order of N.

Applying a microwave of frequency f, we observed the peaks in differential resistance at $I = nef$ (n:integer). This is the consequence of the coupling between the SETO and the microwave electromagnetic field. Figure 3.2.4 shows the differential resistance of sample A as a function of current under microwave irradiation. The excellent agreement of the positions of peaks with nef confirms the existence of coherent SETO in the array.

Figure 3.2.5 shows the result of sample B. The ratios of peaks to the background resistance were less than 2% which were much smaller than those observed in sample A (15-25%).

[4] Due to the twice deposition of Al, the leads on the substrate compose large capacitors. It is one possible reason for the variation of the offset charge that the electrical shock of the switching changes the charge of these capacitors.

[5] The obtained C_0 agrees with the value geometrically estimated. Regarding the island-electrode as the conducting sphere with the same surface area, we obtain $C_0 = 1.8 \times 10^{-17}$F.

These results are explained pretty well within the soliton picture as follows. The potential of the edge electrode polarizes the island-electrodes in the range of λ. When the array is much longer than λ, the effect of environment through the end-electrodes on the soliton motion is small. Thus the solitons keep high space- and time-correlation which lead to coherent SETO of the island-electrodes. The energy for creation of a soliton results in the threshold voltage V_t. In the array with length nearly equal to λ, the voltage-biased end-electrodes tend to fix the potential of all the island-electrodes and reduces the amplitude of the voltage oscillation. The creation energy of a soliton is also diminished because an electron in one end-electrode is attracted by the other more strongly as the array becomes shorter.

3.2.2 Effect of Superconductivity on the SETO

Figure 3.2.6 shows the $\mathrm{d}V/\mathrm{d}I - I$ curves of sample A at low magnetic field with the microwave irradiation. Figure 3.2.7 is the magnetic field dependence of differential resistance at I =40pA. The peaks of differential resistance due to the SETO faded out as the voltage gap in I-V was enhanced by the superconductivity.

At present we cannot explain this phenomenon, although it is clearly related to the superconductivity. As noted before, our junctions do not keep the superconductive phase coherence because of the large charging energy. In very short time, however, they can be treated as nearly coherent and may have AC Josephson oscillation which will be randomized in phase in long periods. The coexistence of a classical SETO and a quantum AC Josephson oscillation will bring a very complicated situation which, at present, we do not know how to cope with.

Delsing *et al.* [10] reported that they observed the peaks of differential resistance due to the SETO in Al/Al-oxide tunnel-junction arrays even without a magnetic field application. In their junctions, I-V characteristics did not change under magnetic field. Probably, for some reasons, the electrodes of their junctions were not superconducting at $H = 0$.

3.3 Conclusion

In this chapter, we studied the effects of the array length and the superconductivity on the SETO in one-dimensional arrays of small tunnel junctions. We obtained the following results:

1. With microwave irradiation, peaks of differential resistance due to the SETO were observed in the normal-state arrays. This implies that the motion of single-electron solitons have space- and time-correlation.

2. The peaks of the differential resistance in the array of $N = 31$ were higher than those in the array of $N = 5$. This shows that in arrays with length nearly equal to the soliton length λ the potential of all the island-electrodes tends to be fixed, which results in weak correlation of solitons.

3. I-V curves of the array of $N = 31$ showed zero current region, while those of the array of $N = 5$ did not. This implies that soliton motion in $N = 5$ array was strongly affected by the end-electrodes.

   Thus, the results are well explained in the context of the soliton picture.

4. The SETO structure was purged away by the superconductivity.

   This phenomenon is very interesting because it may be related to the coexistence of a classical SETO and a quantum AC Josephson effect. At present, clear explanation for this phenomenon is not obtained.

Chapter 4

Influence of Dissipation in One-Dimensional Arrays of Small Josephson Junctions

4.1 Introduction

In chapter 3, we have investigated the single-electron effects in junctions with weak dissipation. In this chapter, we study the influence of dissipation in small Josephson junctions, where the commutation relation between the junction charge and the phase difference will cause various interesting behavior.

In ordinary macroscopic Josephson junctions, the normal state resistance R_N is much smaller than the quantum resistance R_Q and the Josephson coupling energy E_J is much larger than the elementary charging energy E_C and the thermal energy k_BT. In these junctions, the usual Josephson effect is observed and a supercurrent with zero voltage can flow. On the other hand, in very small Josephson junctions where the conditions $E_C \gg E_J$ and $R_N \gg R_Q$ are satisfied, single-electron effects make the zero-bias resistance infinite as

we have seen in chapter 3. It is interesting to study the boundary of these two effects and the behavior of junctions near the boundary.

Many experiments on the influence of dissipation have been performed in connection with the superconductor-insulator(SI) transition in two-dimensional arrays of Josephson junctions. It is known that the critical normal sheet resistance for SI transition is about $R_Q \approx 6.45\text{k}\Omega$ in random systems such as granular films and amorphous films.[11] As for the regular arrays, Geerligs *et al.* [38] reported that the critical normal sheet resistance is about 15kΩ. In these two-dimensional systems, not only charges (Cooper-pairs) but also vortices play an important role. On the other hand, in single junctions and one-dimensional arrays, vortices do not exist, and hence, influence of dissipation is expected to be different from that in two-dimensional arrays.

In this section, we introduce theoretically expected I-V characteristics of small Josephson junctions.

4.1.1 Single-Electron Effects in Single Josephson Junctions without Dissipation

First, we consider single Josephson junctions without dissipation.[13] We assume that the charging energy cannot be ignored. The Hamiltonian of the junction is,

$$H = \frac{Q^2}{2C} - E_J \cos\theta. \tag{4.1}$$

Here Q is the charge stored in the junction, C the capacitance, θ the phase difference between the electrodes. E_J denotes the Josephson coupling energy. Since θ and Q satisfy the commutation relation $[\theta, Q] = 2ei$, we can write

$$Q = \frac{2e}{i}\frac{\partial}{\partial\theta}. \tag{4.2}$$

After all, the Hamiltonian becomes

$$H = -\left(4E_C\frac{\partial^2}{\partial\theta^2} + E_J\cos\theta\right), \tag{4.3}$$

where $E_C = e^2/2C$ is the elementary charging energy. This Hamiltonian is equivalent to that of a particle with mass $(\hbar/2e)^2C$ moving in the sinusoidal potential with height of $2E_J$. The eigenstates are the Bloch states:

$$\psi_{n,Q_x}(\theta + 2\pi) = \exp(i2\pi Q_x/2e)\psi_{n,Q_x}(\theta). \tag{4.4}$$

Here we define the "quasicharge" Q_x corresponding to the quasimomentum in a periodic lattice, which is interpreted as the total charge supplied by the external circuit. The energy level in nearly free electron approximation $E_C \gg E_J$ are shown in Fig 4.1.1. The first Brillouin zone extends over the range $-e \le Q_x \le e$.

Below, we assume that the temperature is so low that the system stays in the ground state. A current $I = dQ_x/dt$ causes a voltage variation $V = \partial E_0/\partial Q_x$, where E_0 is the energy of the ground state. When Q_x reaches e, Cooper-pair tunneling occurs which corresponds to the Bragg reflection in a crystal. This tunneling does not have dissipation since the voltage at $Q_x = e$ is zero. If the junction is biased by a constant current, the voltage oscillates with the frequency,

$$f_B = I/2e. \tag{4.5}$$

This oscillation is analogue to the Bloch oscillation of an electron in a crystal and, therefore, nicknamed accordingly. The Bloch oscillation does not generate dc voltage because the voltage oscillation is symmetric with respect to $V = 0$.

Next let us consider the dc I-V characteristic. We assume that the quasiparticle tunneling is weak, but not zero. At a low current, a quasiparticle tunneling at $Q_x \ge e/2$ causes the SETO and generates a nonvanishing dc voltage. As the current becomes large, the probability that the Bloch oscillation sets in increases. Because the Bloch oscillation does

not accompany the dc voltage, it sometimes causes the negative differential resistance. The structure in the I-V curve due to the SETO and the Bloch oscillation is often called the "Bloch nose".

When the current gets large, tunneling at $Q_x = e$ to the upper band (the Zener tunneling) sets in, which causes the sharp increase of voltage. The overall shape of I-V curve is shown in Fig.4.1.2.

Within this theory, supercurrent with zero voltage seems not to flow as long as E_C is not zero. The supercurrent observed in the experiments is explained as follows: we use the analogy to the particle moving in one-dimensional potential. The ratio of E_J to E_C corresponds to the ratio of the potential energy to the kinetic energy. Therefore, as E_J/E_C gets smaller, the phase difference θ tends to delocalize. When the characteristic time for the delocalization of the phase difference is much longer than the measuring time, the *non-equilibrium* supercurrent will be observed. Thus, the classical Josephson effect are interpreted as a non-equilibrium effect in this theory.[14]

4.1.2 Influence of Dissipation in Single Josephson Junctions

Let us consider a Josephson junction with dissipation. There are two kinds of dissipation: dissipation due to ohmic resistor shunting the junction and dissipation due to quasiparticle tunneling. Generally, quantum-mechanical tunneling itself does not accompany energy dissipation. But in real systems, electrons after tunneling are inelastically scattered and dissipates the energy eV in the electrodes. Hereafter we include this energy dissipation in the tunneling process.

As for the dissipation due to the ohmic shunt resistance, Caldeira and Leggett(CL) proposed to express it by the linear interactions of the junction with the heat bath composed of harmonic oscillators of an infinite number. [15] According to their results, ohmic dissipation reduces the tunneling probability. In the case of Josephson junctions, ohmic

dissipation suppresses the fluctuation of the phase difference. When the dissipation exceeds the critical value, a phase transition of the phase difference occurs and the Josephson supercurrent flows. The critical resistance is universal and equal to the quantum resistance $R_Q = h/(2e)^2 \approx 6.45\mathrm{k}\Omega$.[14] [16]

For the dissipation due to quasiparticle tunneling, Ambegaokar, Eckern and Schön (AES) have obtained the following action from the microscopic Hamiltonian including the charging energy [17]:

$$S[\theta] = \int_0^{\hbar\beta} d\tau \frac{C_G}{2}\left(\frac{\hbar}{2e}\frac{\partial\theta}{\partial\tau}\right)^2 - \int_0^{\hbar\beta} d\tau \int_0^{\hbar\beta} d\tau' \left(\alpha(\tau-\tau')\cos\frac{\theta(\tau)-\theta(\tau')}{2} - \beta(\tau-\tau')\cos\frac{\theta(\tau)+\theta(\tau')}{2}\right), \tag{4.6}$$

where C_G is the geometric capacitance. The α term is related to the dissipation and the β term represents the Josephson coupling term $E_J\cos\theta$ and so-called $\cos\theta$ term of quasiparticle current.[18] Here, we ignore $\cos\theta$ term of quasi-particle current for simplicity.

Next we consider α term in several cases.

If the junction consists of ideal BCS superconductors, the α term (we write α_0) can be rewritten in the form of kinetic energy, which leads to the renormalization of the capacitance [19]

$$C = C_G + \delta C, \delta C = 3\pi\hbar/32\Delta R_N. \tag{4.7}$$

Here R_N is the tunnel resistance in normal state.

In the case of a normal junction ($\Delta = 0$),

$$\alpha_t(\tau) = \alpha_t \frac{\pi^2}{4}\frac{1/\hbar\beta^2}{\sin^2(\pi\tau/\hbar\beta)}, \tag{4.8}$$

$$\alpha_t = \frac{4}{\pi^2}\frac{R_Q}{R_t} \approx \frac{2.6k\Omega}{R_t}, \tag{4.9}$$

where R_t is the tunnel resistance.

Next we consider a non-ideal tunnel junction. The term "non-ideal"means that because, for example, of paramagnetic impurities, the density of states below the superconducting

energy gap is not zero at $T = 0$, and hence, the subgap resistance R_{qp} becomes finite. In this case, we assume that $\alpha = \alpha_0 + \alpha_t$. Here $R_t = R_{qp}$. The action is

$$S[\theta] = \int_0^{\hbar\beta} d\tau \left(\frac{C}{2} \left(\frac{\hbar}{2e} \frac{\partial \theta}{\partial \tau} \right)^2 - E_J \cos\theta \right)$$
$$+ \int_0^{\hbar\beta} d\tau \int_0^{\hbar\beta} d\tau' \alpha_t(\tau - \tau') \left(1 - \cos \frac{\theta(\tau) - \theta(\tau')}{2} \right). \quad (4.10)$$

Guinea and Schön (GS)[20] showed that the partition function for this action is equivalent to that of one-dimensional X-Y model of magnetism and that phase transition of the band structure takes place at the critical α_t. According to the GS theory, quasiparticle tunneling makes the energy band e-periodic and divides the band E_n into E_{n0} and E_{n1}.(Fig. 4.1.3) As dissipation α_t becomes larger, the band width and the difference between E_{n0} and E_{n1} get smaller. After the phase transition E_{n0} and E_{n1} are degenerate. The critical dissipation α_{tc} depends on Q_x and E_J/E_C. Phase diagram is shown in Fig.4.1.4. In region (I) bands degenerate only at $Q_x = \pm e/2$, while in region (III) the bands degenerte for all Q_x. In region (II) bands degenerate in the finite range near $Q_x = \pm e/2$.

The I-V characteristic is influenced by this phase transition. At $T = 0$, the probability of quasiparticle tunneling is

$$\Gamma_{SET}(Q_x) = \frac{2\Delta_{SET}(Q_x)}{e^2 R_{qp}}, \quad (4.11)$$

where

$$\Delta_{SET}(Q_x) = E_{01}(Q_x) - E_{00}(Q_x). \quad (4.12)$$

As dissipation α_t gets larger, Δ_{SET} and Γ_{SET} become smaller and the probability of Bloch oscillations becomes larger. Consequently, dc voltage becomes small. Especially in region (III), dc voltage is infinitesimal.

Their results are summed up as follows.[14]

In the limit $E_J \gg E_C$, the dc voltage is infinite for $\alpha_t > 1$ while Bloch nose structure appears for $\alpha_t < 1$. According to detailed calculation, for larger currents a negative differential resistance appears for $\alpha_t < 0.5$ and positive differential resistance for $0.5 < \alpha_t < 1$.

In the limit $E_J \ll E_C$, for $\alpha_t < 2$ quasiparticle tunneling causes a nonvanishing dc voltage. Detailed calculation shows that at $\alpha_t < 1$ frequent Zener tunneling at low current makes I-V curve similar to that of normal junctions.

The shapes of I-V curves are summarized in Fig.4.1.5.

4.1.3 Dissipative Phase Transition in One-Dimensional Arrays of Small Josephson Junctions

Korshunov[21] considered the AES action for one-dimensional arrays of Josephson junctions and showed that a phase transition between coherent and non-coherent states takes place. The action is

$$S = \sum_j \left(\int_0^{\hbar\beta} d\tau \left(\frac{C_0}{2} \left(\frac{\hbar}{2e} \frac{\partial \varphi_j}{\partial \tau} \right)^2 + \frac{C}{2} \left(\frac{\hbar}{2e} \right)^2 \left(\frac{\partial \varphi_j}{\partial \tau} - \frac{\partial \varphi_{j-1}}{\partial \tau} \right)^2 - E_J \cos(\varphi_j - \varphi_{j-1}) \right) \right)$$
$$+ \sum_j S_D[\varphi_j - \varphi_{j-1}], \quad (4.13)$$

$$S_D[\theta] = \frac{1}{2} \alpha_t \int_0^{\hbar\beta} d\tau \int_0^{\hbar\beta} d\tau' \left(\frac{\sin \frac{1}{4}(\theta(\tau) - \theta(\tau'))}{\tau - \tau'} \right)^2. \quad (4.14)$$

Here C_0 is the self-capacitance of the island-electrode and φ_j the phase of j-th electrode. Dissipation is introduced by the subgap resistance R_{qp}.

The phase diagram in the limit $E_J/E_C \gg 1$ is shown in Fig.4.1.6. In this figure, S_1, S_2 and S_3 are superconducting phase at $T = 0$. Temperature dependence of resistance is different in S_1, S_2 and S_3. In I phase, arrays are insulator where Cooper-pair and quasiparticle cannot tunnel, while resistance is finite due to virtual tunneling in N phase.

4.2 Results and Discussion

4.2.1 Samples

Arrays of tunnel junctions with the same area and the same island-electrodes as those in chapter 3 were fabricated. The number of junctions, N, are 29 or 31. The junction resistance was controlled by changing the pressure of oxygen introduced into the vacuum chamber to form the tunnel barrier. In Table 4.1 we list some important parameters of the samples. Here we estimated the capacitance C and the normal-state resistance R_N by fitting the asymptotic I-V curve in normal state to $V = N(R_N I + e/2C)$. From these parameters, we calculated the elementary charging energy $E_C = e^2/2C$, the Ambegaokar-Baratoff critical current[22] $I_c = \pi\Delta/2eR_N$ and the Josephson coupling energy $E_J = \hbar I_c/2e$, where zero-temperature superconducting energy gap Δ is estimated using the BCS theory.[23] The critical temperature for superconductivity, T_c, is $\approx$ 2K. The self capacitance of the island electrode is $C_0 = 2.4 \times 10^{-17}$F as estimated in chapter 3.

4.2.2 Temperature Dependence of Zero-Bias Resistance

A typical temperature dependence of zero-bias resistance is shown in Fig.4.2.1. We can divide the samples into three groups A-C with respect to the temperature-dependence of the zero-bias resistance, though the change from A to C is indeed continuous. Above T_c, zero-bias resistance of all samples weakly increased with lowering temperature, presumably due to the Coulomb blockade.

Below T_c, the zero-bias resistance of samples 1-5 (group A) increased steeply, while zero-bias resistance of samples 9-12 (group C) stayed at a finite value after monotonic decrease. It is probable that in group C the external noise make the zero-bias resistance finite although ideally the voltage should disappear. The zero-bias resistance of samples

Sample	Group	N	R_N [kΩ]	C [fF]	E_J $\times 10^{-23}$[J]	E_C $\times 10^{-23}$[J]	E_J/E_C
1	A	31	348	0.22	0.045	5.8	0.008
2	A	31	165	0.22	0.095	5.8	0.016
3	A	31	15.3	0.73	1.0	1.8	0.56
4	A	31	7.2	1.4	2.2	0.91	2.4
5	A	29	4.4	1.1	3.6	1.2	3.0
6	B	29	3.1	2.5	5.0	0.51	9.8
7	B	31	3.0	2.7	5.2	0.47	11
8	B	31	2.8	2.7	5.6	0.47	12
9	C	29	2.7	6.4	5.8	0.20	29
10	C	29	2.7	9.0	5.8	0.14	41
11	C	31	1.4	3.0	11	0.42	26
12	C	29	0.49	24	32	0.052	620

Table 4.1: Parameters for the measured samples.

6-8 (group B) exhibited the re-entrant behavior with a minimum around 1K.[1] Figure 4.2.2 shows E_J/E_C vs. R_N for measured junctions. [2]

4.2.3 Current-Voltage Characteristics

Figure 4.2.3 shows the I-V characteristics of samples in group A. Under a perpendicular magnetic field (0.3T) strong enough to destroy the superconductivity, a high-resistance region between sharp current-rising edges appeared around $I = 0$ which is attributed to the Coulomb blockade. The high-resistance region broadened as the magnetic field was lowered toward zero. Both the magnetic-field dependence and the temperature dependence of this broadening indicate that it is due to the superconducting energy gap, though its magnitude is much smaller than the value expected for bulk junctions. (0.4mV $\times$ 31=12.4mV.)

The I-V characteristic of the samples in group B is shown in Fig.4.2.4. There are three features as follows:

1. At the voltage V_m the current rapidly increases. Since differential resistance approaches to R_N above V_m, V_m is attributed to the superconducting gap.

2. There is a current I_m above which the voltage steeply increases. I_m is interpreted as the Zener current where Zener tunneling sets in.

3. There is a high resistance region around the origin. It is attributed to the Coulomb blockade of the single-electron tunneling because of its magnetic field dependence.

[1] The temperature dependence with the re-entrant behavior is similar to that obtained in the films of oxidized tin particles by Kobayashi *et al.*[24] The particle size is 30nm in diameter.

[2] Generally speaking, the tunnel resistance R_N depends on the thickness of the tunnel barrier exponentially and the capacitance C is inversely proportional to it. Then R_N and C satisfy the relation

$$R = a \exp\left(\frac{b}{C}\right),$$

where a and b are constants. Therefore the relation between E_J/E_C and R_N are also on one curve as shown in Fig.4.2.2.

As the magnetic field was increased, this region became wider as shown in Fig.4.2.5 while V_m and I_m decreased monotonically. This is understood by a band picture. With increase of the magnetic field, E_J decreases and the band width of the ground state increases. Accordingly, the energy gain due to single-electron tunneling, Δ_{SET}, and hence the tunnel probability of quasiparticles increase. Therefore, the high-resistance region broadened as the magnetic field became strong. The Zener current I_m decreases because magnetic field makes the band gap narrow. By this magnetic-field dependence, we can conclude that the structure around the origin is the Bloch nose.

I-V curve of samples in group C (Fig.4.2.6) is similar to that in group B except for the absence of the Bloch nose structure. The resistance near the origin is not zero as mentioned in the previous subsection.

Figure 4.2.7 shows the magnetic-field dependence of I-V characteristics. Under weak magnetic fields, the Bloch nose structure did not appeared. When V_m is near zero under strong magnetic field, the zero-bias resistance becomes high. It is attributed not to the Coulomb blockade but the superconducting energy gap.

4.2.4 Comparison with Theories

Just below T_c, $E_J/E_C \ll 1$ and $R_{qp} \approx R_N$ hold. The boundary between the *superconductive* phase where the zero-bias resistance decreases with lowering T and the *insulating* phase where zero-bias resistance increases is 3-4kΩ.

We consider the origin of the re-entrance observed in the samples of group B. The temperature dependent parameters are E_J and R_{qp}.

The Josephson coupling energy, E_J, equals zero at $T = T_c$ and it approaches to the zero-temperature value $E_J = h\Delta/8e^2R_N$ as the temperature decreases. The increase of E_J make the phase difference of the order parameter localize and consequently, the junctions

becomes more superconductive. Therefore, the temperature dependence of E_J does not cause the re-entrance in group B.

On the other hand, the increase of R_{qp} brings the decrease of the influence of dissipation since the strength of dissipation is inversely proportional to R_{qp}. At present, there is no theory which treats the influence of dissipation in tunnel junctions at finite temperatures. For zero temperature, Korshunov have investigated the influence of dissipation due to finite quasiparticle tunneling.[21] We try to compare the experimental results to the Korshunov theory, taking into account the temperature dependence of R_{qp}.

In phase I of the Korshunov theory, both Cooper-pair tunneling and quasiparticle tunneling are blocked. Therefore, the zero-bias resistance will increase with lowering T. In N phase, the zero-bias resistance will decrease for the reason mentioned below.

Figure 4.3.1(a) shows samples' parameters plotted on the Korshunov's phase diagram. Here R_{qp} is replaced with R_N. Just below T_c, E_J is much smaller than the zero-temperature value and R_{qp} is almost same as R_N. As lowering temperature, the point of $\pi\sqrt{C_0 E_J(T)/4e^2}$ vs. $\alpha_t(T)$ sweeps the trajectory as shown in Fig.4.3.1(b).

If the temperature dependence of R_{qp} obeys the BCS theory, R_{qp} increases steeply as

$$R_{qp} = R_N \exp(\Delta(T)/k_B T) \tag{4.15}$$

and the influence of dissipation will not be different between samples in groups A-C at low temperatures.

When we assume that the boundary between N and I lies between group A and B in Fig.4.3.1(a) and that as lowering T points of group B go across the boundary at $\sim$1K while those of group C do not, the experimental results are consistent with the Korshunov theory. Here the critical resistance is 3-4kΩ, which is higher than the expected value of 2.7kΩ.

In Fig.4.3.1(a), regions N and I include the limit $C_0 \to 0$. According to the Korshunov theory, the phase diagram in this limit is the same as that of single junctions. The phases N and I correspond to the phase (I) and (III) in Fig.4.1.4 respectively and the results of

the GS theory are applicable to these phases. In the Korshunov theory for the arrays without external leads, zero-bias resistance of phase N remains finite because virtual tunneling of quasiparticles exists. If arrays are connected to the current source, the Bloch oscillation [3]occurs and zero-bias resistance becomes infinitesimal. This is the case of phase (III) of the GS theory. Thus, the GS theory and the Korshunov theory are consistent in the limit $C_0 \to 0$. Zero-bias resistance of phase N decreases as lowering T because the quasiparticle tunneling due to thermal excitation diminishes.

Now we apply the GS theory to the shape of I-V curves. The I-V curves of group A correspond to 6) in the limit of $E_C \gg E_J$ in Fig.4.1.5. For samples 4 and 5, although E_J is larger than E_C, the small Zener current may makes I-V curves like 6). I-V curves of group B and C correspond to 2) and 1) in the limit $E_J \gg E_C$, respectively. Thus the obtained I-V characteristics are qualitatively explained by the GS theory.

4.3 Conclusion

We studied electrical transport properties of one-dimensional arrays of small Josephson junctions with various R_N and E_J/E_C. We obtained the following results:

1. Just below T_c where $E_J/E_C \ll 1$ and $R_{qp} \approx R_N$ hold, the boundary between the *superconductive* phase where the zero-bias resistance decreases with lowering T and the *insulating* phase where the zero-bias resistance increases is 3-4kΩ.

2. The temperature dependence of zero-bias resistance of samples with 2.8k$\Omega \le R_N \le$ 3.1kΩ and $9.8 \le E_J/E_C \le 12$ shows re-entrant behavior. When we assume that there exists the subgap resistance with nonideal temperature dependence, the results are qualitatively explained by the Korshunov and GS theories.

[3]Numerical calculations in ref.[25] show that the Bloch oscillation takes place and that the Bloch nose structure appears in arrays of Josephson junctions.

3. The Bloch nose structure was found in I-V curves of samples with $2.8\text{k}\Omega \leq R_N \leq 3.1\text{k}\Omega$ and $9.4 \leq E_J/E_C \leq 11$. This is an evidence for the existence of the Bloch oscillation in one-dimensional arrays of Josephson junctions.

Chapter 5

Electrical Transport in Two-Dimensional Arrays of Small Tunnel Junctions

5.1 Introduction

In two-dimensional arrays of small tunnel junctions, the charge Kosterlits-Thouless (KT) transition and the vortex KT transition (in Josephson junction arrays) are expected. The former takes place in normal junction arrays and in Josephson junction arrays with $E_C \gg E_J$, and the latter in arrays with $E_J \gg E_C$. The vortex KT transition are observed in many experiments[26], while there is no experiment of artificially-fabricated junctions which supports the charge KT transition.

Possible reasons for the absence of the charge KT transition are i) it is difficult to separate the charge KT transition from the other single-electron effects, ii) because of the finite screening length within which charges interact logarithmically, the charge KT transition is washed out. The purpose of this experiment is to study the properties of

electrical transport in arrays larger than those studied so far.

5.1.1 Single-Electron Effects in Two-Dimensional Arrays

Let us consider a regular square array of tunnel junctions with junction capacitance C and self capacitance C_0 of island electrode as shown in Fig.5.1.1. We assume that the tunnel resistance R is so large that the effects of dissipation are negligible.

The charge $Q(x,y)$ and the potential $\phi(x,y)$ on the island-electrode at (x,y) satisfy the Poisson equation,

$$Q(x,y) = C_0\phi(x,y)+C(4\phi(x,y)-\phi(x-1,y)-\phi(x+1,y)-\phi(x,y-1)-\phi(x,y+1)). \quad (5.1)$$

We assume that an excess charge exists only on the island-electrode at $(0,0)$. In continuum approximation for island-electrodes far from the origin $r = \sqrt{x^2+y^2} \gg 1$, equation(5.1) becomes

$$\nabla^2 \phi(r) - \Lambda^{-2}\phi(r) = 0, \quad (5.2)$$

where $\Lambda = \sqrt{C/C_0}$ is the screening length. The solution is

$$\phi(r) = \frac{e}{2\pi C} K_0\left(\frac{r}{\Lambda}\right). \quad (5.3)$$

Here K_0 is the zero-order modified Bessel function. If $r \gg \Lambda$, $\phi(r)$ decays exponentially. For $r \ll \Lambda$,

$$\phi(r) = -\frac{e}{2\pi C}\ln\frac{r}{\Lambda}. \quad (5.4)$$

Thus an excess charge induces logarithmic potential within the range of Λ.

The I-V characteristic of this array shows two features like that of one-dimensional arrays.[27] First is the threshold voltage for electron injection. Because electrons are repulsed from the lateral edges, it takes minimum value V_t^{2D} for the middle rows:

$$V_t^{2D} = \begin{cases} \frac{e}{2C}\left(1-\frac{2}{\pi}\right)\left(\frac{C}{C_0}\right)^{1/2}, & \text{for } C_0 \ll C, \\ \frac{e}{2C_0}, & \text{for } C_0 \gg C. \end{cases} \quad (5.5)$$

Second is the offset voltage of I-V curve at large current:

$$V_{off}^{2D} = \begin{cases} Ne/4C & \text{(global rule)}, \\ Ne/2C & \text{(local rule)}, \end{cases} \quad (5.6)$$

where N is the number of junction in current direction. Here global rule is the limit where the time for charge redistribution after tunneling is much shorter than the time electron is allowed to spend in the forbidden state by the uncertainty relationship. This time is estimated to be $\hbar/E_C$ because the energy difference between the states before and after the tunneling is of the order of E_C. In this limit electron motion far from the edge electrodes does not increase the electrostatic energy of the array. Local rule is the opposite limit.[28]

5.1.2 Charge KT Transition

Let us consider the limit $C_0 = 0$. Interaction between charges depends on the mutual distance logarithmically. In this case, the system is regarded as two-dimensional Coulomb gas of charge and anticharge, which leads to KT transition.

The KT transition is characterized as the breakdown of the topological order.[29][30] Below a critical temperature T_{KT}, the correlation function of the order parameter is proportional to the power of the distance and "quasi"long range order exists. Here, all of the topological excitations, vortices, bind into vortex-antivortex pairs. Above T_{KT}, the correlation of the order parameter is broken by single vortices and antivortices, and disordered state emerges.

In the case of the charge KT transition, vortices correspond to charges. Below T_{KT}, all charges and anticharges bind in pairs. Because the pairs are not pulled or repelled by an electric field, the zero-bias resistance of the array becomes infinite. Above T_{KT} the number of free charges increases and the resistance becomes finite.

The transition temperature T_{KT}^n for normal junctions and T_{KT}^* for Josephson junctions

are[31]

$$T_{\rm KT}^{\rm n} = E_{\rm C}/4\pi\epsilon_{\rm C}, \tag{5.7}$$

$$T_{\rm KT}^{\rm s} = E_{\rm C}/\pi\epsilon_{\rm C} \tag{5.8}$$

where $\epsilon_{\rm C} \approx 1.16$ for square lattice.

The density of free charges close to the transition ($0 \leq (T - T_{\rm KT})/T_{\rm KT} \ll 1$) is square-root-cusp type and given by

$$n_{\rm f}(T) = K \exp\left(\frac{-2b}{\sqrt{T/T_{\rm c} - 1}}\right), \tag{5.9}$$

where K and b are constants of order 1. The resistance is inversely proportional to $n_{\rm f}$ and given by

$$R(T) = \left(\frac{N}{W}\right) K \exp\left(\frac{2b}{\sqrt{T/T_{\rm c} - 1}}\right), \tag{5.10}$$

where N (W) are the number of junctions parallel (perpendicular) to the current.

As the voltage becomes larger below $T_{\rm KT}$, the charge and the anticharge are pulled in opposite directions stronger and finally, the pair separates into a free charge and a free anticharge. This mechanism makes the I-V characteristic nonlinear as is expected in the vortex KT transition.[32] If we write $I \propto V^{a(T)}$, the exponent $a(T)$ is proportional to $1/T$ below $T_{\rm KT}$ and jumps from 3 to 1 at $T_{\rm KT}$, which corresponds to the "universal jump of the superfluid density". Above $T_{\rm KT}$, $a(T) = 1$.[33]

5.1.3 Effects of Dissipation and Josephson Coupling Energy

We summarize the effects of dissipation and finite Josephson coupling energy on the charge KT transition.

Fazio *et al.* calculated the effect of dissipation on $T_{\rm KT}^{\rm n}$ using AES-type action. [34][35]

As the dissipation becomes strong, electrons tunnel frequently and the fluctuation of charges in the island-electrodes gets large, which reduces the critical temperature.

The results are

$$\frac{T_{\rm KT}^{\rm n}}{T_{\rm KT}^{\rm n0}} = 1 - 0.1 \times \frac{\pi^2}{4}\alpha_{\rm t} \quad \text{for very small dissipation,} \tag{5.11}$$

$$\frac{\pi^2}{4}\alpha_{\rm t} \approx 0.45\left(1 - \frac{\pi}{4}\frac{T_{\rm KT}^{\rm n}}{T_{\rm KT}^{\rm n0}}\right) \quad \text{for strong dissipation.} \tag{5.12}$$

Here $T_{\rm KT}^{0}$ denotes the transition temperature without the correction. Equation(5.12) implies that the charge KT transition does not occur in arrays with the tunnel resistance $R_{\rm t} < 15{\rm k}\Omega$.

Josephson coupling energy $E_{\rm J}$ also increases the fluctuation of the charges in the island-electrodes because of the uncertainty relationship between the phase and the charge. When $E_{\rm J}$ is small, the decrease of the critical temperature is expressed as[34]

$$\frac{T_{\rm KT}^{\rm s}}{T_{\rm KT}^{\rm s0}} = 1 - 0.98\left(\frac{E_{\rm J}}{E_{\rm C}}\right)^2. \tag{5.13}$$

5.1.4 Experiments on the Charge KT Transition

Mooij *et al.*[31] measured the temperature dependence of the resistance of 190×60 junction array. They showed that the temperature where the resistance diverged in superconducting state was almost 4 times larger than that in normal state, which agrees with the prediction for the charge KT transition. But because the temperature dependence was the activation type

$$R \propto \exp(-\frac{E_{\rm a}}{T}), (E_{\rm a}: \text{activation energy}), \tag{5.14}$$

rather than the predicted square-root-cusp type(eq.(5.10)), it is doubtful whether it is the evidence of the charge KT transition. Tighe *et al.* also measured the temperature dependence of the resistance of 70×50 junction arrays.[36] They concluded that it was complete activation type and that there was no sign of the charge KT transition.

5.2 Results and Discussion

5.2.1 Sample Design and Characteristics

For the observation of the charge KT transition, the screening length $\Lambda = \sqrt{(C/C_0)}$ must be as large as possible. There are three ways for this purpose: i) To enlarge the junction area. ii) To thin the oxide film. iii) To make small island-electrodes. The methods i) and ii) are not applicable, since they decrease the tunnel resistance, and consequently suppress the charge KT transition as expected in the previous section. Therefore, we make the area of the island-electrode as small as possible.(Fig.5.2.1(a))

In the experiment, we fabricated a regular square lattice with 400 junctions long and 331 junctions wide. Leads for voltage measurement are attached to island-electrodes which is 50 junctions apart from the end-electrode.(Fig.5.2.1(b)) The junction area is about $0.01(\mu m)^2$ and the normal-state resistance per one junction is 60kΩ. This value is so large that we can neglect the effects of the dissipation. By fitting the I-V curve at high voltage to $V = NRI + Ne/2C$, we estimated the capacitance C to be 1.7×10^{-15}F. From these values, we obtain the Josephson coupling energy E_J=0.18K and the elementary charging energy E_C=0.56K. The self capacitance is estimated to be 5×10^{-17}F [1] and the screening length Λ to be 6 junctions.

5.2.2 Temperature Dependence of Resistance

Figure 5.2.2 shows the temperature dependence of resistance at V=0.2mV. The electrodes were superconducting. As will be mentioned in the next subsection, the I-V characteristic was ohmic around and below this voltage. In this figure, the resistance was proportional to the inverse of temperature except within the range of $1/T = 1 - 5$. We fit the R-T curve within the range of $1/T = 1 - 5$ to the square-root-cusp type temperature dependence

[1] We estimated C_0 by regarding the island-electrode as the metal disk with the same surface area.

(5.10). The result is $T_{KT}^* = (0.13 \pm 0.01)$K, which agrees with the theoretical value 0.14K obtained from E_J and E_C. (Eq.(5.8)(5.13))

The deviation from the square-root-cusp behavior at $1/T > 5 (T < 0.2K)$ comes from the finite-Λ effect. As the distance between charges becomes larger than Λ, the interaction falls off exponentially. Therefore, the temperature dependence of resistance deviates from the square-root-cusp type (5.10) which is obtained in the limit $\Lambda \to \infty$. The temperature T_{dev} where the deviation appears is estimated as

$$\frac{1}{\pi(\frac{\Lambda}{2})^2} = K \exp\left(\frac{-2b}{\sqrt{T_{dev}/T_c - 1}}\right). \tag{5.15}$$

From this equation, we obtain $T_{dev}/T_{KT} \approx 1.6$, which agrees with the experimental value $T_{dev}/T_{KT} = 1.5$. Detailed calculation by Minnhagen[37] gives $T_{dev}/T_{KT} \approx 1.4$.

Thus, the temperature dependence of resistance is attributed to the charge KT transition mechanism with finite screening length.

The activation energy at low temperatures where the temperature dependence of the resistance is activation type is 0.63K. This corresponds to the creation energy of single Cooper-pairs. According to Tighe *et al.*[36], the energy for creating a Cooper-pair and an anti-Cooper-pair by a Cooper-pair tunneling is $(2e)^2/2(2C) = 2E_C$ in the limit $C_0 = 0$. Therefore, the activation energy is $E_C = 0.55K$. In real junctions, the effective capacitance deviates from $2C$ because of the nonvanishing C_0, and consequently the activation energy also deviates from E_C. In the experiment by Tighe *et al.*[36], the activation energy above 0.3K is the sum of the creation energy of single electrons and the superconducting energy gap. This result does not agree with ours. In their arrays, the Zener tunneling due to a small value of E_J/E_C may suppress the Cooper-pair tunneling, and in addition, the motion of electron may be strongly affected by the end-electrodes because the array length is only about 4 times larger than the screening length.

5.2.3 Current-Voltage Characteristics

The I-V characteristic at 0.055K in zero magnetic field is shown in Fig.5.2.3. The voltage corresponding to the superconducting energy gap is estimated from the BCS theory as

$$eV_\Delta = 2N \times 1.76 k_B T_c. \tag{5.16}$$

Using $T_c = 1.9$K and N=300, we obtain $V_\Delta = 170$mV. In Fig5.2.2 we find the structure corresponding to V_Δ.

The theory tells that the probability of the Zener tunneling at current i is[38]

$$\Gamma_z = \exp\left(-\frac{\pi}{8}\frac{E_J^2}{E_C}\frac{e}{\hbar i}\right). \tag{5.17}$$

The Zener tunneling becomes significant near a current

$$\begin{aligned} I &= N \times i \\ &= N \times \frac{\pi}{8}\frac{E_J^2}{E_C}\frac{e}{\hbar} \\ &= 160\text{nA}. \end{aligned}$$

Therefore we attribute the steep increase of voltage above 75nA to Zener tunneling.

Around the origin, the high resistance region due to the Coulomb blockade and the Bloch nose structure are noticeable.

This high resistance region shows a large temperature dependence as shown in Fig.5.2.4. At the voltage of the order of 1mV, I-V curves are nonlinear while below 1mV they approach the ohmic behavior. The results of fitting of this nonlinear part to $I \propto V^a$ are shown in Fig.5.2.5. The temperature where $a(T) = 3$ is $\approx$0.14K. This agrees with T_{KT}^* obtained above.

In the ideal KT transition, the relation $I \propto V^a$ is satisfied at all voltages and a jumps from 3 to 1 at the critical temperature. This is not the case in ours. This is to be attributed to the effect of finite screening length. In the ideal KT transition where the screening length is infinite, free charges are produced at the critical temperature by the breaking of pairs with an infinite distance, which needs infinitesimal energy. When the screening length is finite, there exists no pair with an infinite distance and free charges will be produced at higher temperatures than in the ideal case. Therefore, above the critical temperature I-V curve will deviate from that of ideal case.

Above T_{dev}, the free charges can interact with each other logarithmically. In the experiment, $a(T) \approx 1$ above T_{dev}, which agrees with the prediction for the ideal case. Thus the temperature range where I-V curves deviate from those in the ideal case can be attributed to the effect of finite screening length. But the reasons why $a(T)$ takes values between 1 and 3 at $T_{KT} < T < T_{dev}$ and why I-V curves are nonlinear only in finite voltage range are still unknown.

5.2.4 Experiments on the Normal Arrays

A piece of experimental evidence for the charge KT transition is that the transition temperature in zero magnetic field where the electrodes are superconducting is about 4 times larger than that in a magnetic field strong enough to break the superconductivity. Unfortunately, we failed to obtain clear results of the normal junction array in this experiment, partly because the expected transition temperature was too low.

5.3 Conclusion

We studied the electrical transport properties in a two-dimensional array of small Josephson junctions with high resistance. The results are

1. The square-root-cusp behavior of temperature dependence of resistance was observed in finite temperature range. The obtaind critical temperature agrees with the theoretical value. The temperature at which deviation from the square-root-cusp behavior

occured also agrees with the theoretical value which takes account of the effect of finite screening length.

2. The overall shape of I-V characteristic is attributed to the single electron effects in Josephson junctions. Nonlinear I-V characteristics are seen in finite voltage range. The results of fitting of this nonlinear region to $I \propto V^a$ are explained as the KT-like behavior with finite screening length.

Chapter 6

Conclusion

In this thesis, we studied on three subjects concerning the single-electron effects in small tunnel junction arrays.

In chapter 3, we studied the effects of the array length and the superconductivity on the SETO in one-dimensional arrays of small tunnel junctions. We obtained the following results:

1. With microwave irradiation, peaks of differential resistance due to the SETO were observed in the normal-state arrays. This implies that the motion of single-electron solitons have space- and time-correlation.

2. The peaks of the differential resistance in the array of $N = 31$ were higher than those in the array of $N = 5$. This shows that in arrays with length nearly equal to the soliton length λ the potential of all the island-electrodes tends to be fixed, resulting in weak correlation of solitons.

3. I-V curves of the array of $N = 31$ showed zero current region, while those of the array of $N = 5$ did not. This implies that soliton motion in the $N = 5$ array was strongly affected by the end-electrodes.

Thus, the results are well explained in the context of the soliton picture.

4. The SETO structure was purged away by the superconductivity.

   This phenomenon is very interesting because it may be related to the coexistence of a classical SETO and a quantum AC Josephson effect. At present, clear explanation for this phenomenon is not obtained.

In chapter 4, we studied electrical transport of small Josephson junction array with various R_N and E_J/E_C. We obtained the following results:

1. Just below T_c where $E_J/E_C \ll 1$ and $R_{qp} \approx R_N$ hold, the boundary between the *superconductive* phase where the zero-bias resistance decreases with lowering T and the *insulating* phase where the zero-bias resistance increases is 3-4kΩ.

2. The temperature dependence of zero-bias resistance of samples with 2.8k$\Omega \leq R_N \leq$ 3.1kΩ and $9.8 \leq E_J/E_C \leq 12$ shows reentrant behavior. A possible reason is that there exists *nonideal* subgap resistance. The results are qualitatively explained by the Korshunov and GS theories.

3. The Bloch nose structure was found in I-V curves of samples with 2.8k$\Omega \leq R_N \leq$ 3.1kΩ and $9.4 \leq E_J/E_C \leq 11$. This is an evidence for the existence of the Bloch oscillation in one-dimensional arrays of small Josephson junctions.

In chapter 5, we studied the electrical transport properties in a two-dimensional array of small Josephson junctions with high resistance. The results are

1. The square-root-cusp behavior of temperature dependence of resistance was observed in finite temperature range. The obtaind critical temperature agrees with the theoretical value. The temperature at which deviation from the square-root-cusp behavior took place also agrees with the theoretical value which takes account of the effect of finite screening length.

2. The overall shape of I-V characteristic is attributed to the single electron effects in Josephson junctions. Nonlinear I-V characteristics are seen in a finite voltage range. The results of fitting of this nonlinear region to $I \propto V^a$ are explained as the KT-like behavior with finite screening length.

Acknowledgment

I would like to express my sincere thank to my supervisor Professor Shun-ichi Kobayashi, for stimulating advices and discussions throughout this work. I also express my gratitude to him for proof reading this manuscript.

I would like to thank Professor S. Katsumoto and Professor F. Komori for fruitful discussions and advices both on the interpretation of the experimental results and on the experimental techniques. Useful advices by Professor S. Ikehata, Professor Y. Ootuka, Dr. H.Shimada, Dr. Y.Shimazu and Dr. R.Yagi are also gratefully acknowledged.

Finally, I thank all the members of Kobayashi-Ikehata group and Ootuka group for their encouragement during this work.

Bibliography

[1] G. J. Dolan, Appl. Phys. Lett. **31** 337 (1977).

[2] D. V. Averin and K. K. Likharev, J. Low. Temp. Phys. **62** 345 (1985).

[3] D. B. Haviland, L. S. Kuzmin P. Delsing and T. Claeson, Europhys. Lett. **16** 103 (1991).

[4] S. Shapiro, Phys. Rev. Lett. **11** 80 (1963).

[5] L. Solymer, *Superconductive Tunneling and Applications* (Chapman and Hall Ltd, London, 1972)

[6] N. S. Bakhalov, G. S. Kazacha, K. K. Likharev and S. I. Serdyukova, Zh. Eksp. Teor. Fiz. **95** 1010 (1988) [Sov. Phys. JETP **68** 581(1989)].

[7] K. K. Likharev, S. I. Serdyukova, G. S. Kazacha and N. S. Bakhavalov. IEEE Trans. Magn. **25** 1436 (1989).

[8] P. W. Anderson, in *Lectures on the Many Body Problem*, Ravello 1963, Vol II, edited by E. R. Caianello (Academic Press, New York, 1964) p.113.

[9] M. Tinkham, *Introduntion to Superconductivity*, (McGraw-Hill, New York, 1975).

[10] P. Delsing, K. K. Likharev, L. S. Kuzmin and T. Claeson Phys. Rev. Lett. **63** 1861 (1989).

[11] See for instance, S. Kobayashi, in *Selected Topics in Superconductivity*, edited by L. C. Gupta and M. S. Multani (World Scientific, Singapore, 1993), p.371.

[12] L. J. Geerligs, M. Peters, L. E. M. de Groot, A. Verbruggen and J. E. Mooij, Phys. Rev. Lett. **63** 326 (1989).

[13] K. K. Likharev and A. B. Zorin, J. Low Temp. Phys. **59** 347 (1985).

[14] G. Schön and A. D. Zaikin, Phys. Rep. **198** 237 (1990), and references therein.

[15] A. O. Caldeira and A. J. Legett, Phys. Rev. Lett. **46** 211 (1981); Ann. Phys. (NY) **149** 374 (1983).

[16] M. P. A. Fisher and W. Zweager, Phys. Rev. **B32** 6190 (1985).

[17] V. Ambegaokar, U. Eckern and G. Schön, Phys. Rev. Lett. **48** 1745 (1982); U. Eckern, G. Schön and V. Ambegaokar, Phys. Rev. **30** 6419 (1984).

[18] See for instance, A. Barone and G. Paternò, *Physics and Applications of the Josephson Effect*, (John Weily & Sons, New York, 1982).

[19] V. Ambegaokar, in *Percolation, Localization, and Superconductivity*, Proceedings of the Nato Advanced Study Institutre, Les Arcs, France, 1983, edited by A. M. Goldman and S. A. Wolf (Plenum, New York, 1984), p. 43.

[20] F. Guinea and G. Schön, Europhys. Lett. **1** 585 (1986).

[21] S. E. Korshunov, Europhys. Lett. **9** 107 (1989); *Erratum* **9** 839 (1989).

[22] V. Ambegaokar and A. Baratoff, Phys. Rev. Lett. **10** 486 (1963); *Erratum* **11** 104 (1963).

[23] J. Bardeen, L. N. Cooper and J. R. Schrieffer, Phys. Rev. **108** 1175 (1957).

[24] S. Kobayashi, Y. Tada and W. Sasaki, Physica **107B** 129 (1981).

[25] U. Geigenmuller and G. Schön, in Proc. of the 3rd Intl. Symposium Foundations of Quantum Mechanics, p.276, Tokyo (1989).

[26] For instance, H. S. J. van der Zant, H. A. Rijken and J. E. Mooij, J. Low Temp. Phys. **79** 289 (1990); *ibid* **82** 67 (1991).

[27] N. S. Bakhvalov, G. S. Kazacha, K. K. Likharev and S. I. Serdyukova, Physica **B173** 319 (1991).

[28] U. Geigenmüller and G. Schön, Europhys. Lett. **10** 765 (1989).

[29] J. M. Kosterlitz and D. J. Thouless, J. Phys. **C6** 1181 (1973).

[30] V. L. Berezinskii, Zh. Eksp. Teor. Fiz. **59** 907 (1970) [Sov. Phys. JETP **32** 493 (1971)].

[31] J. E. Mooij, B. J. Wees, L. J. Geerligs, M. Peters, R. Fazio and G. Schön, Phys. Rev. Lett. **65** 645 (1990).

[32] B. I. Halperin and D. R. Nelson, J. Low Temp. Phys. **36** 599 (1979).

[33] J. E. Mooij and G. Schön, in *Single Charge Tunneling*, edited by H. Grabert and M. H. Devoret (Plenum Press, New York, 1992), p.275.

[34] R. Fazio and Schön, Phys. Rev. **B43** 5307 (1991)

[35] R. Fazio, in *Quantum Coherence in Mesoscopic Systems*, edited by B. Kramer (Plenum Press, New York, 1991), p.571.

[36] T. S. Tighe, M. T. Tuominen, J. M. Hergenrother and M. Tinkham, Phys. Rev. **47** 1145 (1993).

[37] P. Minhagen, Rev. Mod. Phys. **59** 1001 (1987).

[38] J. M. Ziman, *Principles of the Theory of Solids* (Cambridge University Press, Cambridge, 1972)

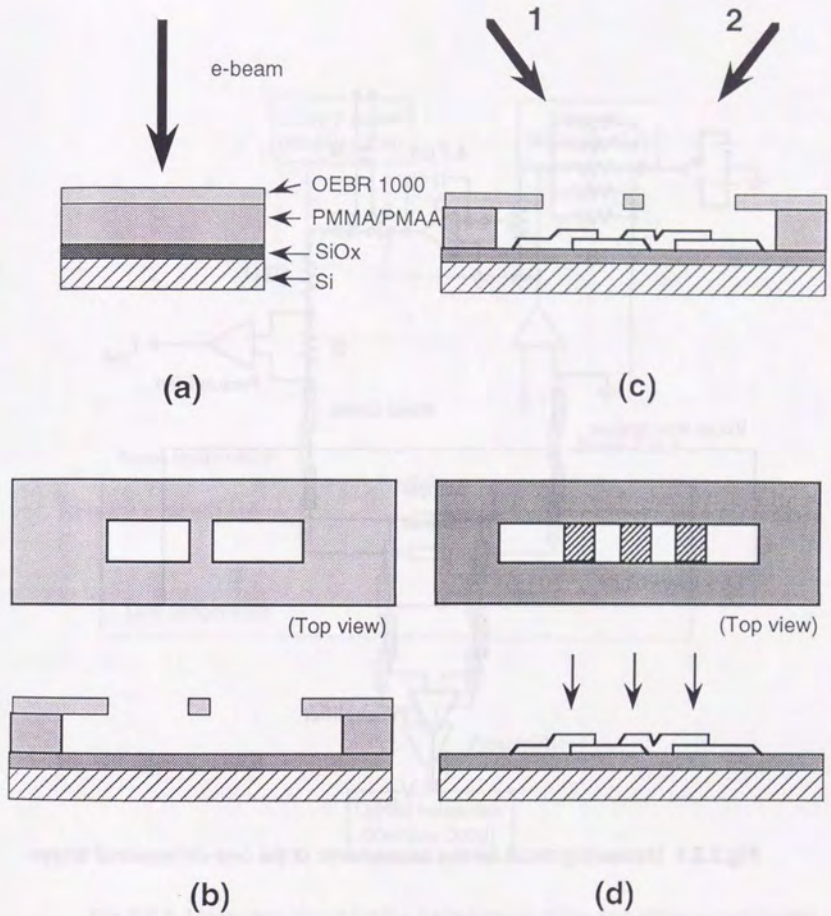

Fig.2.1.1 Junction fabrication method. (a) Two-layer resists are exposed to the electron beam. (b) After the developments, suspended bridge structure is fabricated. (c) Al is evaporated from two different directions. (d) After the lift-off process, junctions are fabricated where the two Al films are overlapped. The hatched areas in the top view and the arrows in the sectional view indicate the positions of the tunnel junctions.

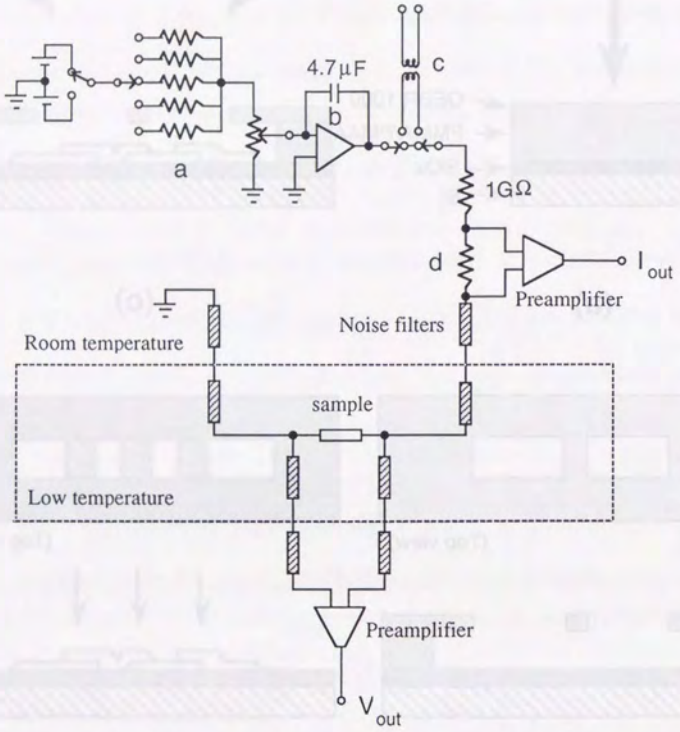

Fig.2.2.1 Measuring circuit for the experiments of the one-dimensional arrays.

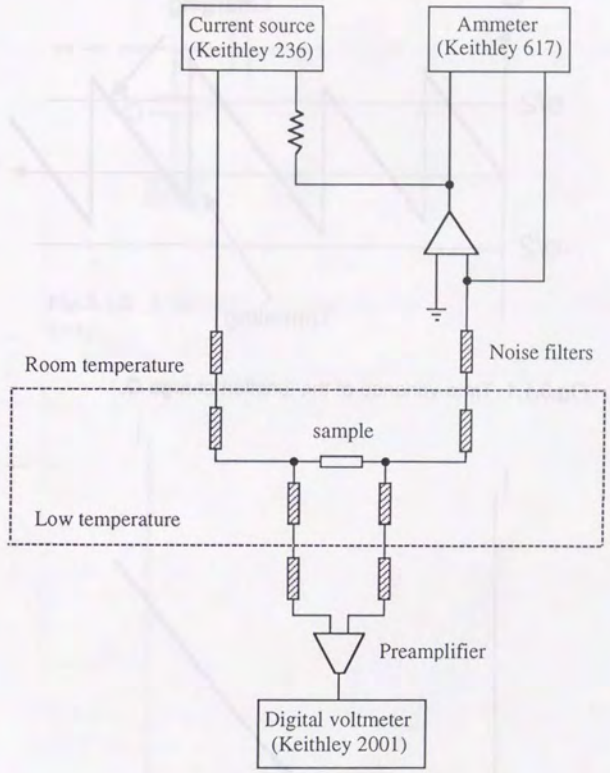

Fig.2.2.2 Measuring circuit for the experiments of the two-dimensional arrays.

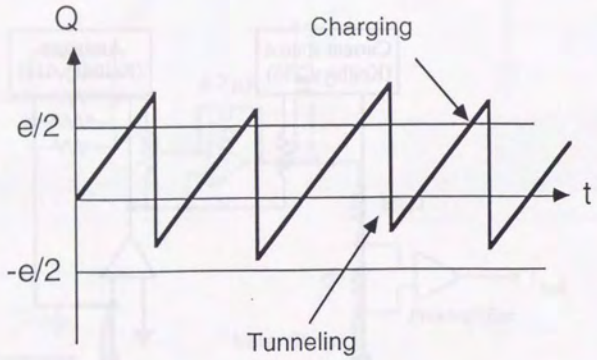

Fig.3.1.1 Time variance of the junction charge *Q*.

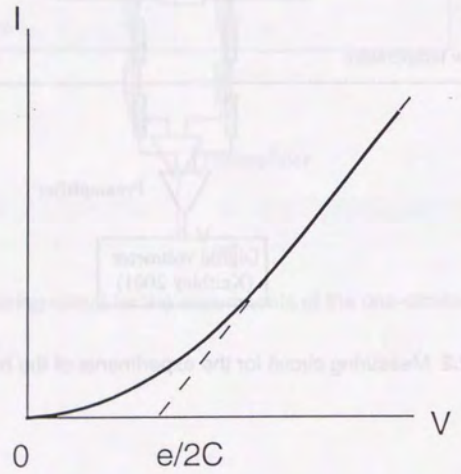

Fig.3.1.2 A schematic view of the *I-V* characteristic of a normal single junction.

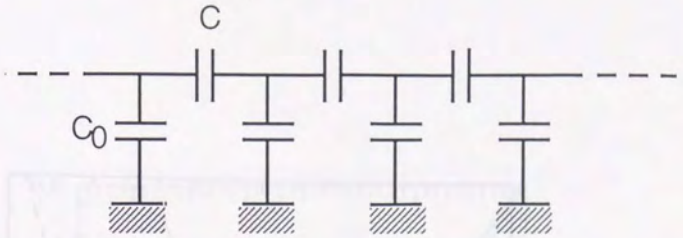

Fig.3.1.3 A schematic equivalent circuit of a one-dimensional junction array.

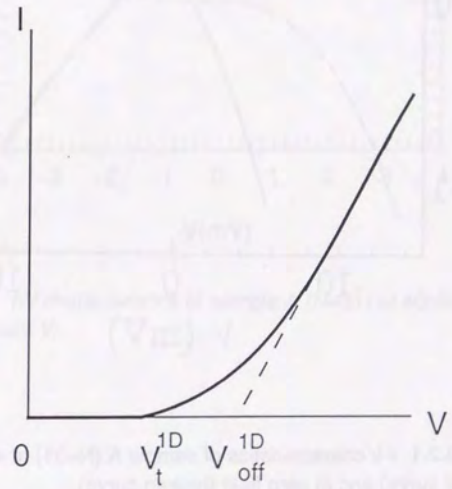

Fig.3.1.4 A schematic view of the *I-V* characteristic for a one-dimensional junction array.

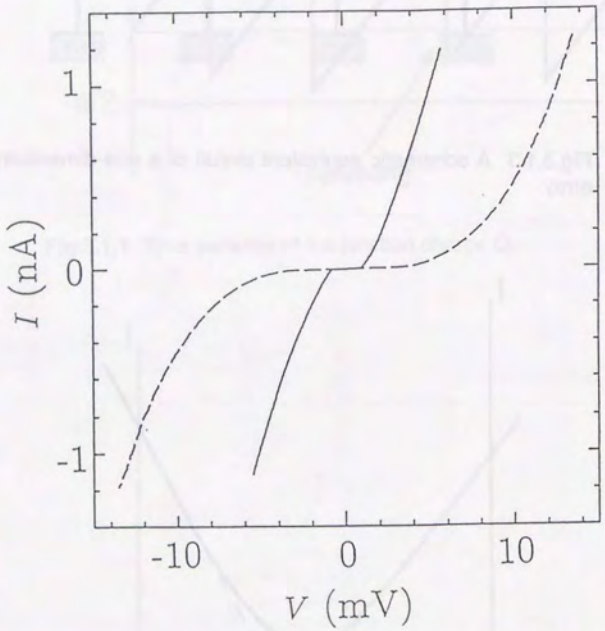

Fig.3.2.1 *I-V* characteristics of sample A (N=31) at 40mK in 3 Tesla (solid curve) and in zero field (broken curve).

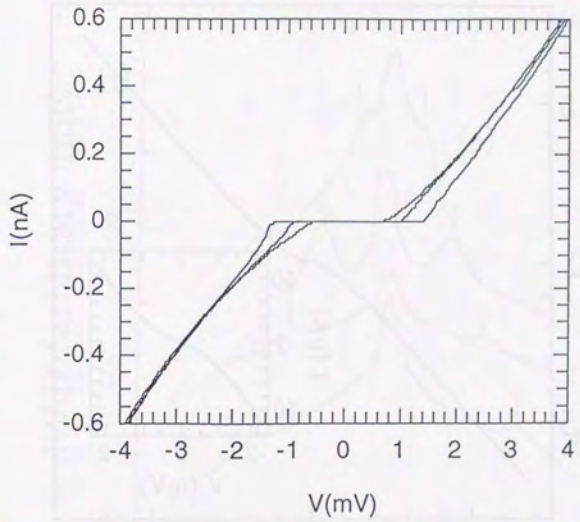

Fig.3.2.2 *I-V* characteristics of sample A (N=31) at 40mK in 3 Tesla with different V_t.

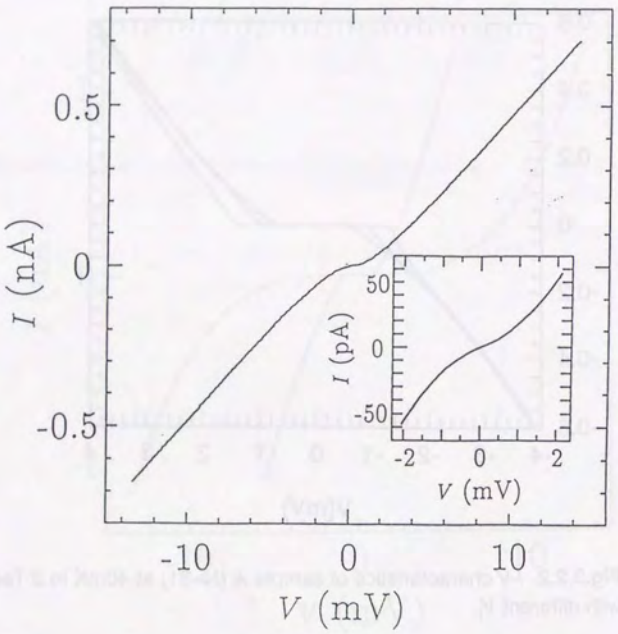

Fig.3.2.3 *I-V* characteristic of sample B (N=5) at 40mK in 3 Tesla. The inset is the enlargement near the origin.

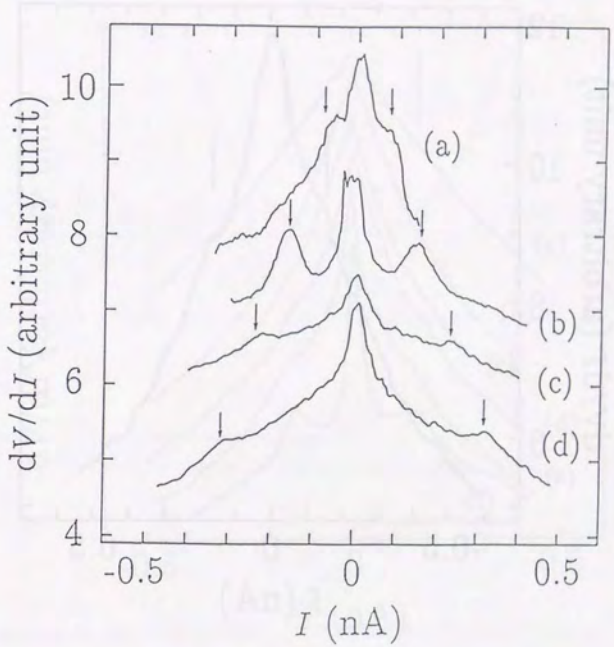

Fig.3.2.4 Differential resistance vs. *I* of sample A for microwave frequencies *f*= (a) 0.5GHz, (b) 1GHz, (c) 1.5GHz, (d) 2GHz. The allows indicate the positions of $I=\pm ef$. Curves (a),(b) and (c) are offset by 3, 2, and 1 in d*V*/d*I*-*I* axis for clarity.

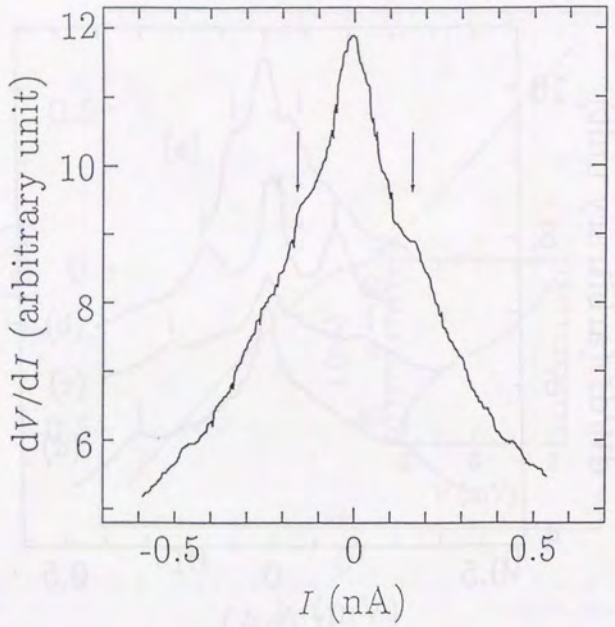

Fig.3.2.5 Differential resistance vs. I of sample B for f=1GHz. The allows indicate the positions of $I = \pm ef$.

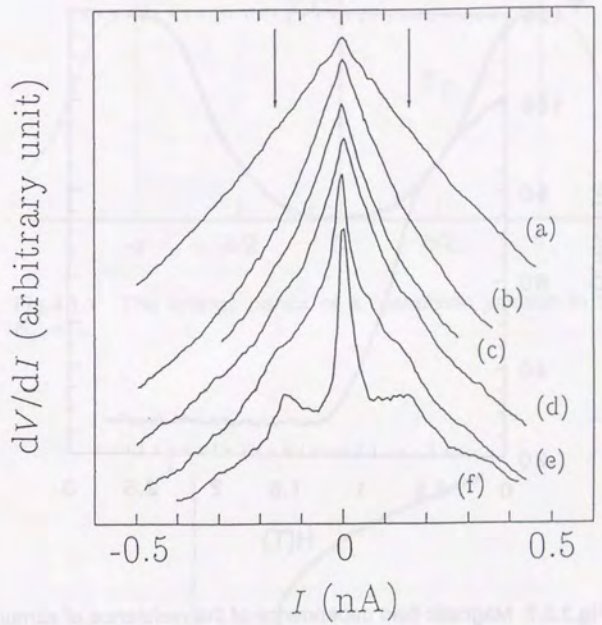

Fig.3.2.6 Magnetic field dependence of dV/dI vs. I for sample A with the microwave irradiation of f=1GHz. The magnetic fields are (a) 0.5 T, (b) 0.8 T, (c) 0.9 T, (d) 1 T, (e) 1.2 T, (f) 1.5 T. The allows indicate the positions of $I = \pm ef$. The peaks at $I = \pm ef$ vanish below 1 T. The voltage gap in I-V curve was enhanced by superconductivity below 1.2 T. The curves are offset in dV/dI axis for clarity.

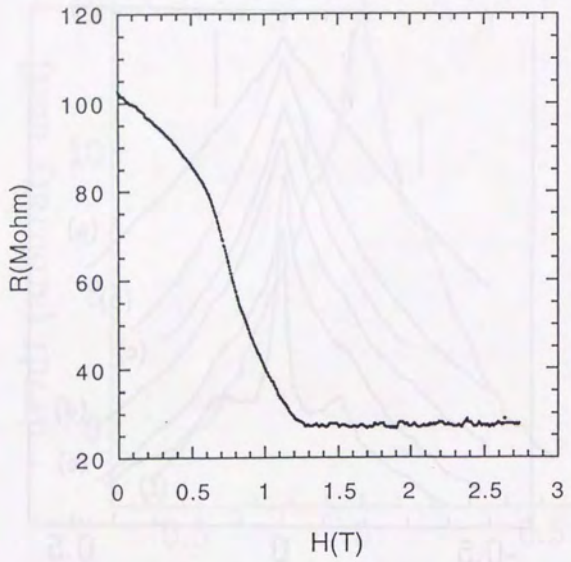

Fig.3.2.7 Magnetic field dependence of the resistance of sample A at *I*=40pA.

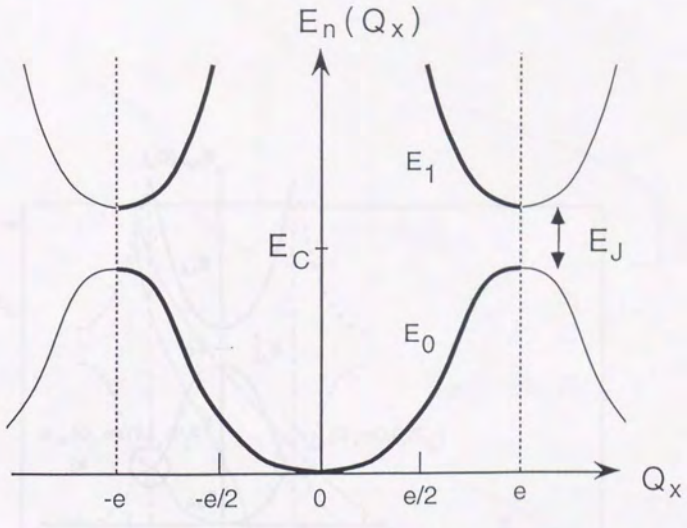

Fig.4.1.1 The energy bands of a Josephson junction in the limit of $E_C >> E_J$.

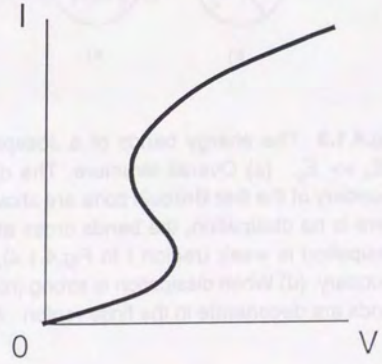

Fig.4.1.2 A schematic view of the *I-V* characteristics for a small Josephson junction.

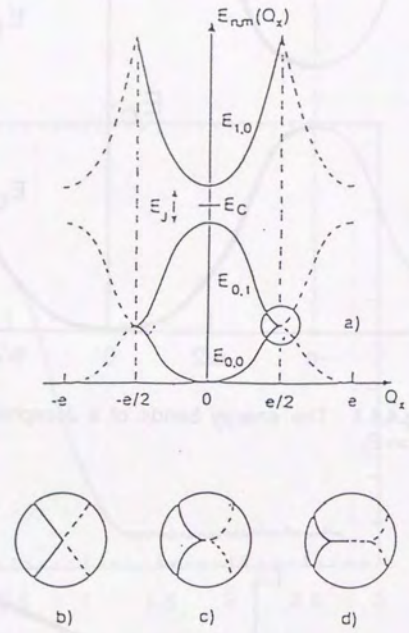

Fig.4.1.3 The energy bands of a Josephson junction in the limit of $E_J >> E_C$. (a) Overall structure. The detail structures near the boundary of the first Brillouin zone are shown in (b) to (d). (b) When there is no dissipation, the bands cross at the boundary. (c) When dissipation is weak (region I in Fig.4.1.4), the bands touch at the boundary. (d) When dissipation is strong (region II and III in Fig.4.1.4) bands are degenerate in the finite region. After [11].

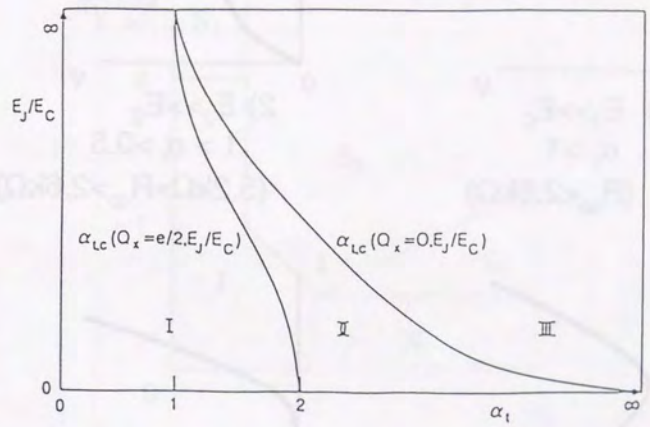

Fig.4.1.4 The phase diagram for the phase transition due to quasiparticle tunneling. After [11].

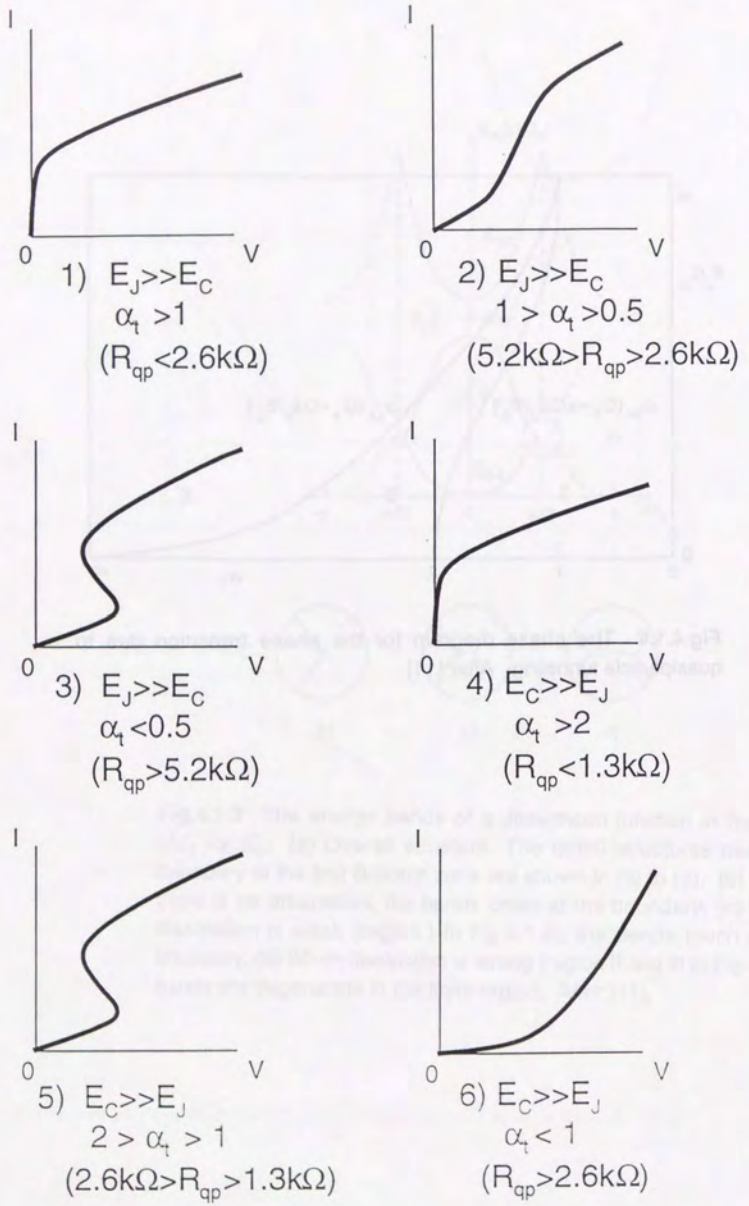

Fig.4.1.5 Schematic view of the *I-V* characteristics of single Josephson junctions with various R_{qp} in the limit of $E_J >> E_C$ and $E_C >> E_J$.

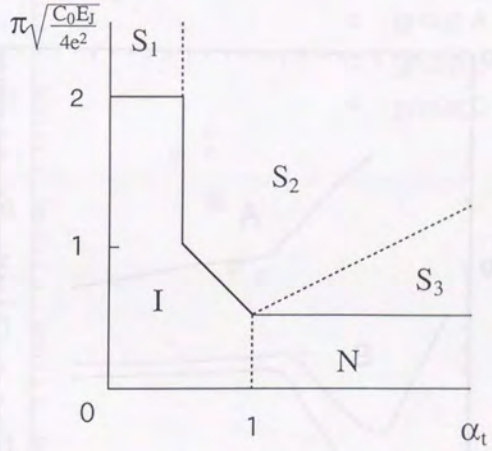

Fig.4.1.6 Phase diagram of one-dimensional arrays of small Josephson junctions in the limit of $E_J / E_C >> 1$ at $T=0$.

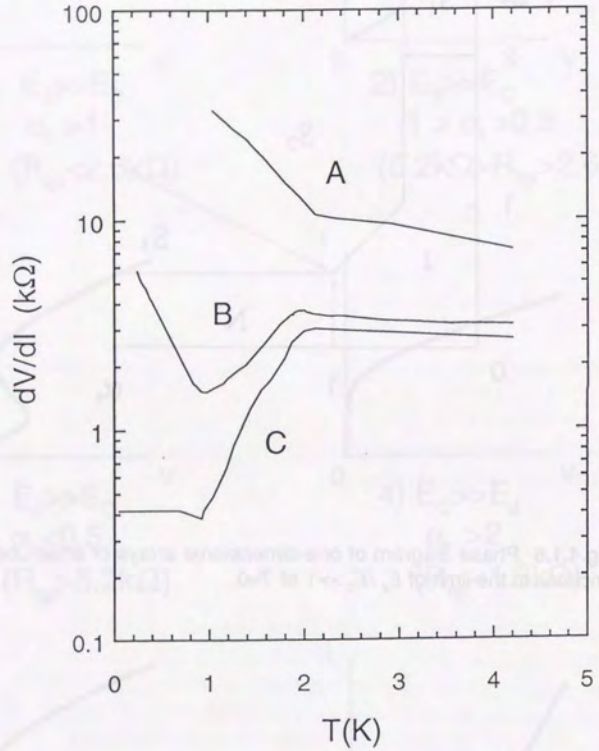

Fig.4.2.1 Typical temperature dependence of zero-bias resistance for samples 4 (in group A),6 (in group B) and 9 (in group C).

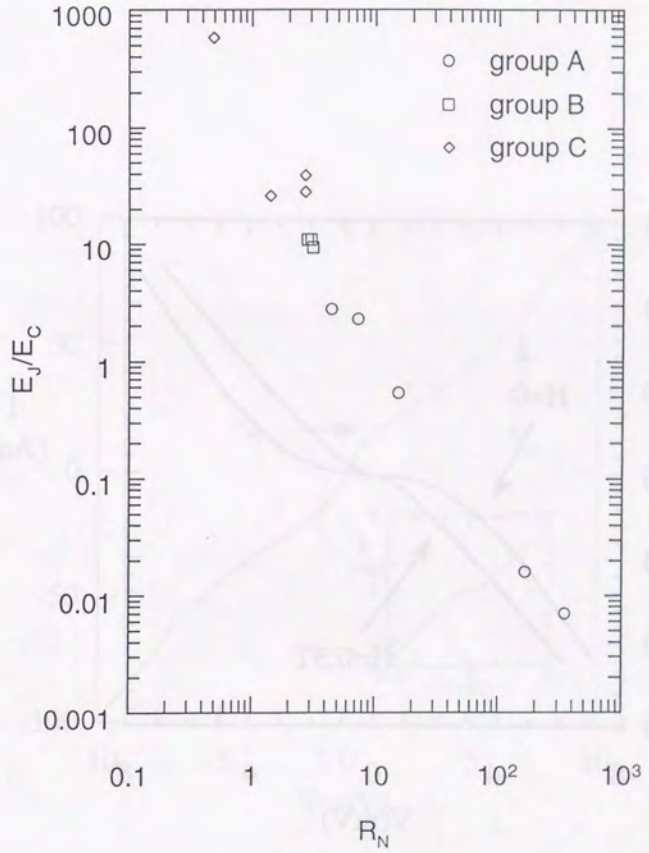

Fig.4.2.2 E_J/E_C vs. R_N for measured samples.

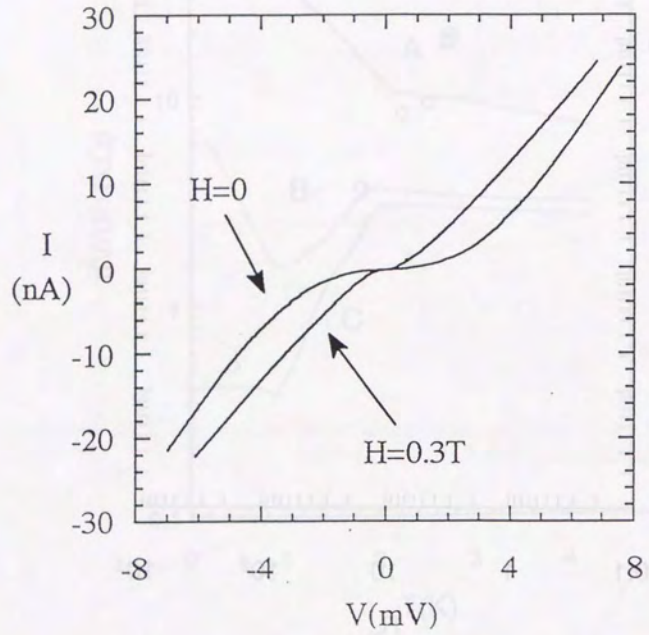

Fig.4.2.3 *I-V* characteristics of sample 4 (group A) in normal state (*H*=0.3T) and superconducting state(*H*=0) at 0.1 K.

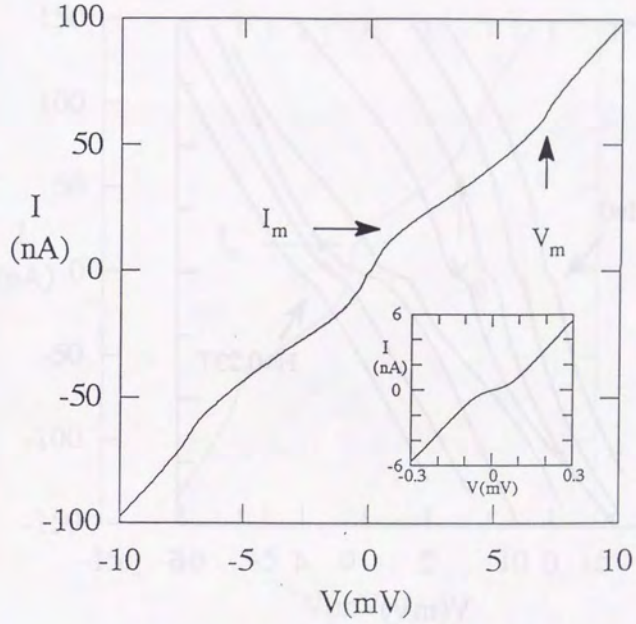

Fig.4.2.4 *I-V* characteristic of the sample 7 (group B) at 40mK. The inset is the enlargement near the origin.

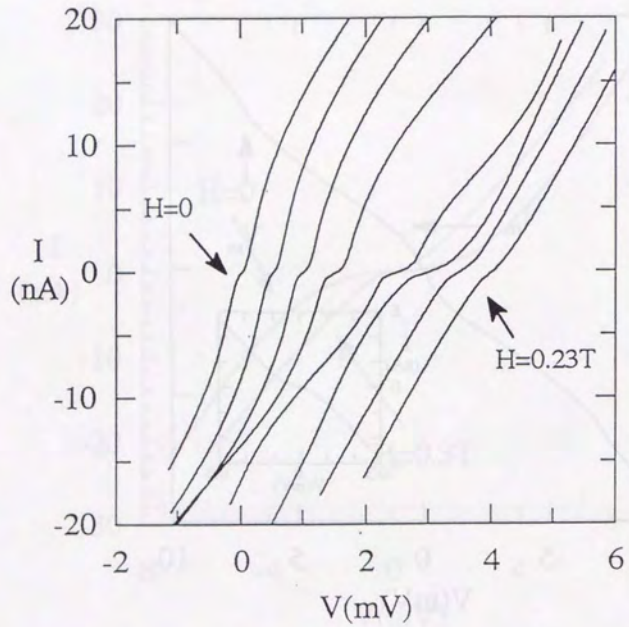

Fig.4.2.5 Magnetic field dependence of *I-V* characteristics for sample 7 (group B). The magnetic fields are 0, 0.03, 0.05, 0.08, 0.1, 0.13, 0.16,0.23T from the left to the right. Curves except H=0 are offset in *V* for clarity.

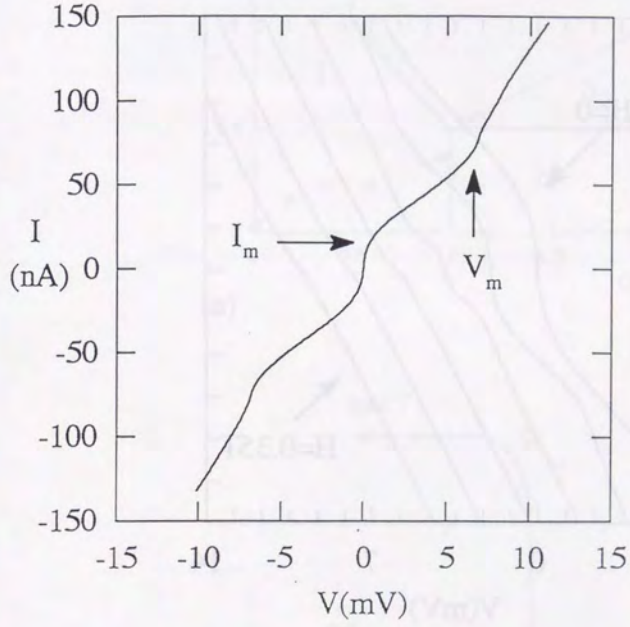

Fig.4.2.6 *I-V* characteristic of sample 10 (group C) at 40mK.

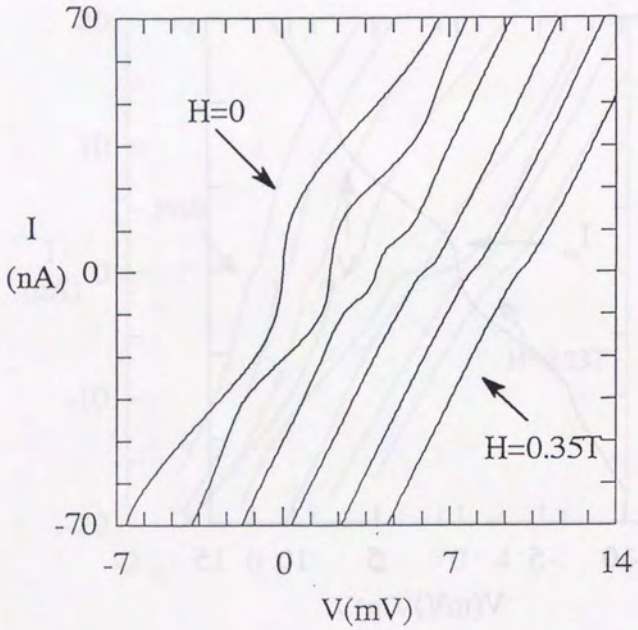

Fig.4.2.7 Magnetic field dependence of *I-V* characteristics for sample 10 (group C). The magnetic fields are 0, 0.1, 0.15, 0.2, 0.25, 0.35T from the left to the right. Curves except H=0 are offset in *V* for clarity.

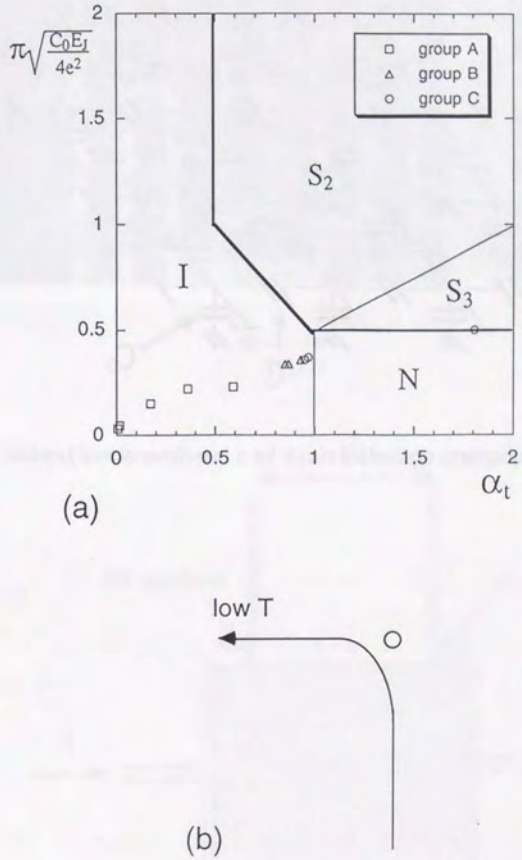

Fig.4.3.1 (a)Parameters for measured samples plotted in the Korshunov's phase diagram. (b) Temperature variation of the sample's parameters (curve). Circle indicates the point in (a).

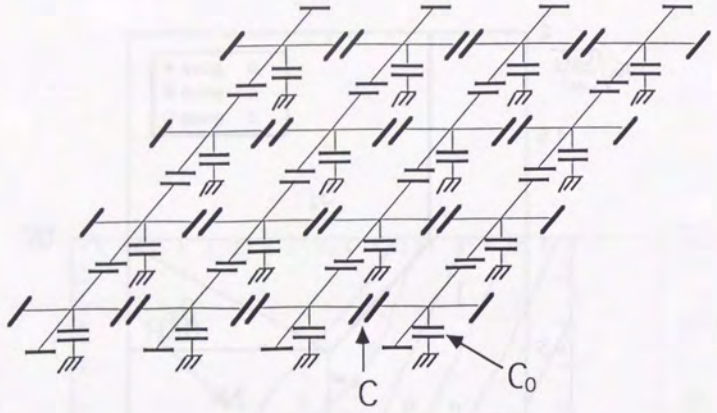

Fig.5.1.1 A schematic equivalent circuit for a two-dimensional junction array.

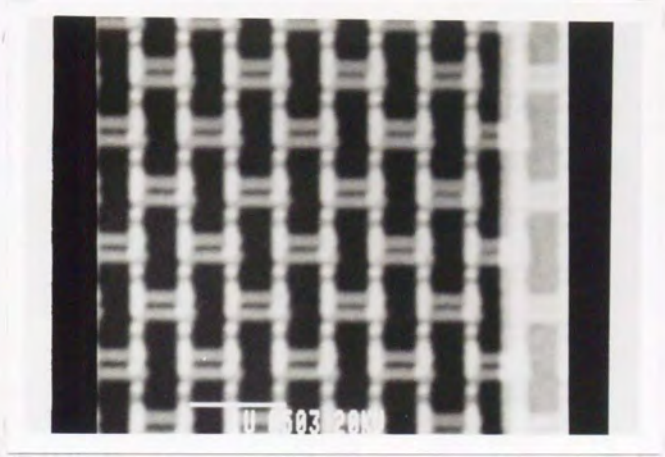

Fig.5.2.1 (a) An scanning electron microscope picture of Au/Au prototype of the two-dimensional array. (b) A schematic view of the arrangement of electrodes in two-dimensional array.

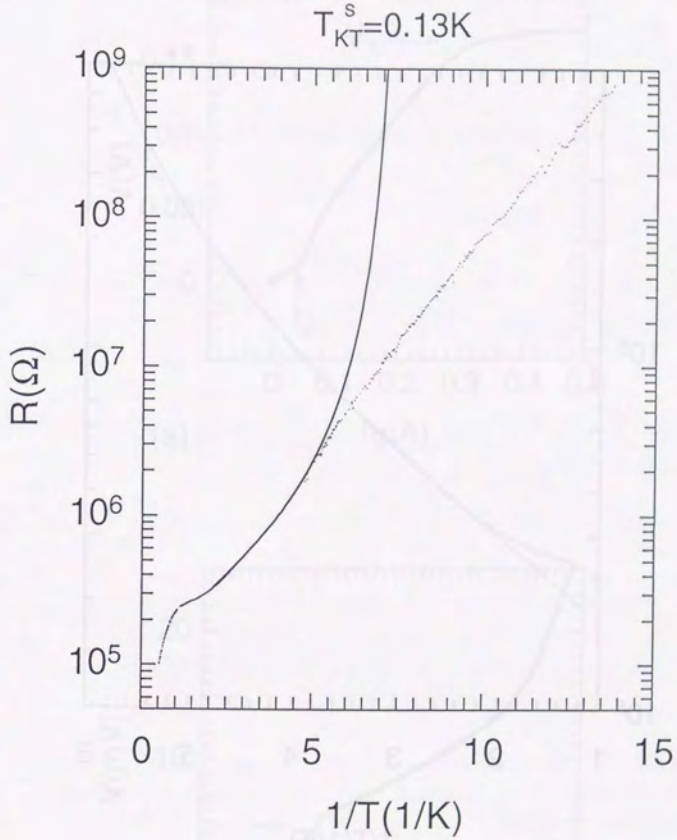

Fig.5.2.2 (a)Temperature dependence of resistance at *V*=0.2mV in zero magnetic field. Solid line shows the result of the fitting to the square-root-cusp temperature dependence.

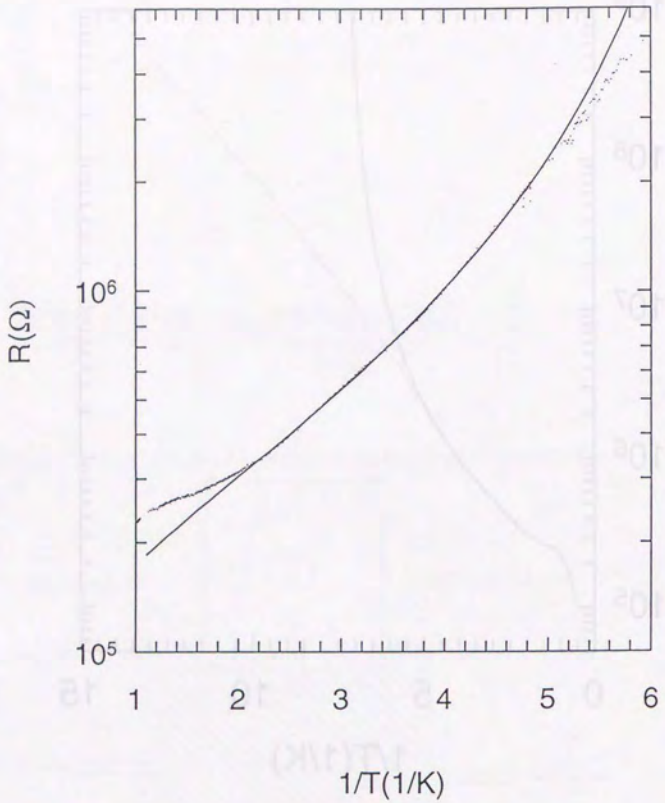

Fig.5.2.2 (b)Enlargement of Fig.5.2.2(a).

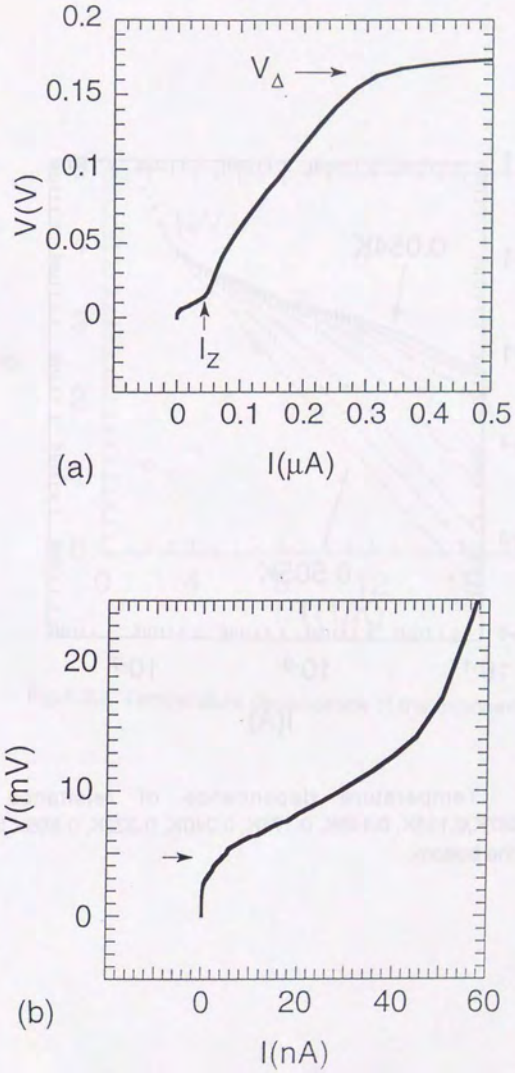

Fig.5.2.3 (a) *I-V* characteristic of the array at 54mK. (b) The enlargement near the origin.

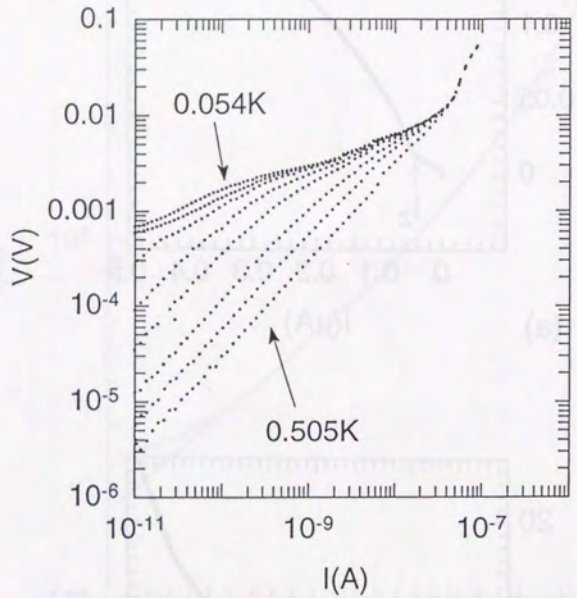

Fig.5.2.4 Temperature dependence of reisitance at 0.054K,0.087K,0.115K, 0.146K, 0.177K, 0.240K, 0.322K, 0.505K from the top to the bottom.

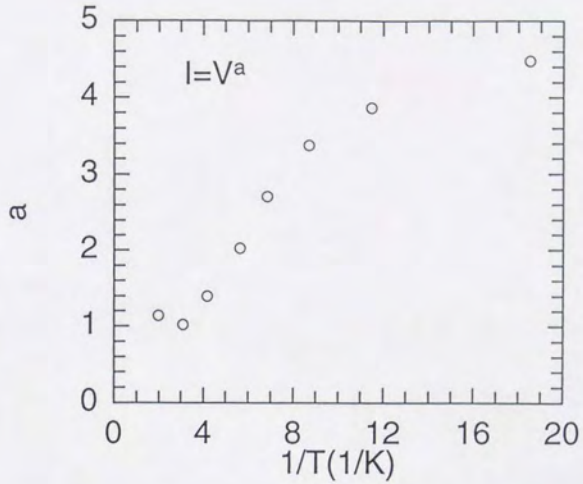

Fig.5.2.5 Temperature dependence of the exponent *a*.